Multi-modality imaging with structure-promoting regularisers

Matthias J. Ehrhardt

Institute for Mathematical Innovation, University of Bath, UK

m.ehrhardt@bath.ac.uk

Abstract

Imaging with multiple modalities or multiple channels is becoming increasingly important for our modern society. A key tool for understanding and early diagnosis of cancer and dementia is PET-MR, a combined positron emission tomography and magnetic resonance imaging scanner which can simultaneously acquire functional and anatomical data. Similarly in remote sensing, while hyperspectral sensors may allow to characterise and distinguish materials, digital cameras offer high spatial resolution to delineate objects. In both of these examples, the imaging modalities can be considered individually or jointly. In this chapter we discuss mathematical approaches which allow to combine information from several imaging modalities so that multi-modality imaging can be more than just the sum of its components.

1 Introduction

Many tasks in almost all scientific fields can be posed as an inverse problem of the form

$$Ku = f \tag{1}$$

where K is a mathematical model that connects an unknown quantity of interest u to measured data f. The task is to recover u from data f under the model K. In practice this task is difficult because of measurement errors in the data f and inaccuracies in the model K. Moreover, in many cases the model (1) lacks information we have at hand about the unknown quantity u such as its regularity. In this chapter we are interested in the situation when have a-priori knowledge about the "structure" of u from a second measurement v which we want to exploit in the inversion. Throughout this chapter we will refer to v as the *side information*. Intuitively, this is the case when u and v describe different properties of the same geometry (in medicine: anatomy). We will be more precise in Section 2 where we discuss mathematical models for structural similarity. The two notions we will discuss in detail that the edges of the two images u and v having similar 1) locations [1–5] and 2) directions [3, 5–16]. Real-world examples for these mathematical models are numerous as we will see in the next section.

1.1 Application examples

Historically the first application where information from several modalities was combined was positron emission tomography (PET) and magnetic resonance imaging (MRI) in the early 1990s [17]. Sharing information between two different imaging modalities is motivated by the fact that all images will be highly influenced by the same underlying anatomy, see Figure 1. Since single-photon emission computed tomography (SPECT) imaging is both mathematically and physically similar to PET imaging, most of the proposed models can be directly translated and often models are proposed for both modalities simultaneously, see e.g. [18–21]. Over the years there always has been research in this direction, see e.g. [18–20, 22–34], which was intensified with the advent of the first simultaneous PET-MR scanner in 2011 [35], see e.g. [4, 5, 11–13, 36–43].

The same motivation applies to other medical imaging techniques, for example multi-contrast MRI, see e.g. [10, 44–48]. In multi-contrast MRI multiple acquisition sequences are used to acquire data of the same patient, see Figure 2 for a T_1- and a T_2-weighted image with share anatomy. Other special cases are the combination of anatomical MRI (e.g. T_1-weighted) and magnetic particle imaging [14], functional MRI (fMRI) and anatomical MRI [49] as well as anatomical (^{1}H) and fluorinated gas (^{19}F) MRI [50]. A

Figure 1: **PET-MR and PET-CT.** A low resolution functional PET image (left) is to be reconstructed with the help of an anatomical MRI (middle) or CT image (right). As is evident from the images, all three images share many edges due to the same underlying anatomy. Note that the high soft tissue contrast in MRI makes it favourable over CT for this application. Images curtesy of P. Markiewicz and J. Schott.
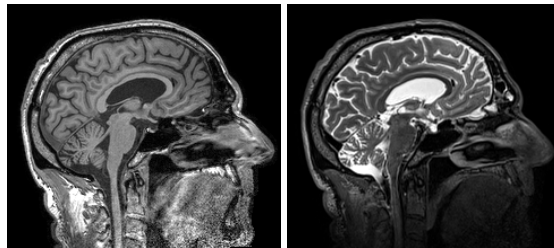

Figure 2: **Multi-contrast MRI.** The same MRI scanner can produce different images depending on the acquisition sequence such as T_1-weighted (left) and T_2-weighted images (right). Images courtesy of N. Burgos.

related imaging task is quantitative MRI (such as Magnetic Resonance Fingerprinting [51]) [52–55] where one aims to reconstruct quantitative maps of tissue parameters (e.g. T_1, T_2, proton density, off-resonance frequency), but regularisers coupling these maps have not been used to date. The idea to couple channels has also been used for parallel MRI [56].

Starting from the 1990s, mathematical models were developed that make use of the expected correlations between colour channels of RGB images [58–60], see Figure 3. Research in this field is still very active today, see e.g. [2, 8, 61–64].

In remote sensing observations are often available from multiple sensors either mounted on a plane or on a satellite. For example a hyperspectral camera with low spatial resolution and a digital camera with higher spatial resolution may be used simultaneously, see Figure 4. This situation naturally invites for the fusion of information, see [15, 65–71] and references therein. In some situations the response of the cameras to certain wavelengths is (assumed to be) known such that the data can be fused making use of this knowledge. This is commonly referred to as, see e.g. *pansharpening* [68–70]. It is important to note that this assumption is sometimes not fulfilled and many of the aforementioned algorithms are flexible enough to fuse data in this more general situation.

Dual and spectral computed tomography (CT) is becoming increasingly popular in (bio-) medical imaging and material sciences due to its ability to distinguish different materials which would not be

Figure 3: **Color imaging.** The color image (left) is composed of three color channels (right) all of which show similar edges due to the same scenery. Images courtesy of M. Ehrhardt.
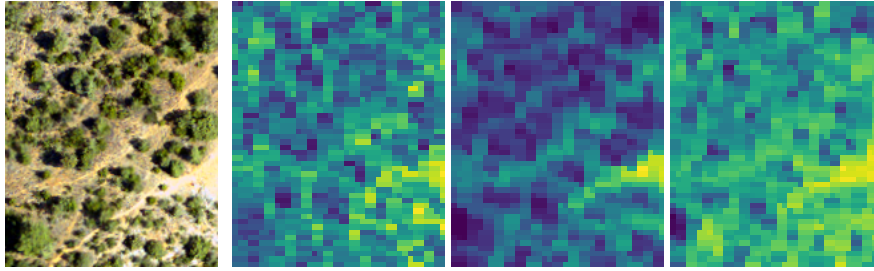
Figure 4: **Hyperspectral imaging + photography.** A nowadays common scenario is that multiple cameras are mounted on a plane or satellite for remote sensing. While one camera carries spectral information (right), the other has high spatial resolution (left). Images courtesy of D. Coomes.
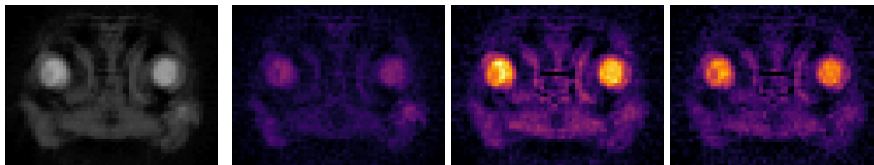

Figure 5: **Spectral CT.** Standard (white-beam) CT on the left and three channels (28, 34 and 39 keV) of spectral CT on the right of an iodine-stained lizard head reconstructed by CIL [57]. The spectral channels clearly show a large increase in intensity from 28 to 34 keV, thereby revealing the presence, location and concentration of iodine. Images courtesy of J. Jorgensen and R. Warr.

possible using a single energy, see Figure 5. Since the energy channels have a very different signal-to-noise ratio, coupling them within the reconstruction allows to transfer information from high signal to low signal channels [9, 72–74].

In geophysics, the coupling between modalities has been used to model similarity between electrical resistivity and seismic velocity [6, 7], estimating conductivity from multi-frequency data [75], inverting gravity and seismic tomography [75] and controlled-source electromagnetic resistivity inversion [76]. For an overview and more details on examples in geophysics see in [3, 77] and references therein.

Ideas from multi-modality imaging have recently also been used for art restoration. When a canvas is painted on both sides, an x-ray image shows the superposition of both paintings. The x-ray information can then be separated using photos of both sides of the canvas [78].

Other examples that were considered in the literature are combining anatomical information and electrical impedance tomography [16, 79], CT and MRI [80], photo-acoustic and optical coherence tomography [81], x-ray fluorescence and transmission tomography [82] and various channels in multi-modal electron tomography [83]. The combination of various imaging modalities into one system may eventually lead to what is sometimes referred to as *omni-tomography* [84].

Image reconstruction with side information is mathematically similar to multi-modal image registration and thus it is not surprising that both fields share a lot of mathematical models, see e.g. [85–88].

1.2 Variational regularisation

Inverse problems of the form (1) can be solved using variational regularisation, i.e. framed as the optimisation problem

$$u_\alpha \in \arg\min_u \mathcal{D}(Au, f) + \alpha \mathcal{R}(u). \tag{2}$$

Here the *data fidelity* $\mathcal{D} : Y \times Y \to \mathbb{R}_\infty := \mathbb{R} \cup \{\infty\}$ measures how close the estimated data Au fits the acquired data f. The *regulariser* (also referred to as the *prior*) $\mathcal{R} : X \to \mathbb{R}_\infty$ defines which properties of the image u we favour and which we do not. The trade-off between data fitting and regularisation can be chosen using the *regularisation parameter* $\alpha > 0$. Problems of this form have been extensively studied, see for instance [89–93] and references therein.

Three popular regularisers for imaging are the *squared H^1-semi norm* (H^1), the *total variation* (TV) [94, 95] and the *total generalised variation* (TGV) [96–98]. It is common to model images as functions

3

$u : \Omega \subset \mathbb{R}^d \to \mathbb{R}$. If u is smooth enough, then these regularisers are defined as

$$H^1(u) = \int_\Omega |\nabla u(x)|^2 \, dx \tag{3}$$

$$TV(u) = \int_\Omega |\nabla u(x)| \, dx \tag{4}$$

$$TGV(u) = \inf_\zeta \int_\Omega |\nabla u(x) - \zeta(x)| + \beta |E\zeta(x)| \, dx . \tag{5}$$

Here $\nabla u : \Omega \to \mathbb{R}^d, [\nabla u]_i = \partial_i u$ denotes the gradient of u, $E\zeta : \Omega \to \mathbb{R}^{d \times d}, [E\zeta]_{i,j} = (\partial_i \zeta_j + \partial_j \zeta_i)/2$ denotes the symmetrised gradient of a vector-field $\zeta : \Omega \to \mathbb{R}^d$, see [98] for more details, and $|\cdot|$ denotes the Euclidean/Frobenius norm. For TV and TGV it is of interest to develop other formulations which are well-defined even when u is not smooth. For simplicity, we do not go into more detail in this direction but refer the interested reader to the literature, e.g. [95, 96].

All three regularisers promote solutions with different smoothness properties. H^1 promotes smooth solutions with small gradients everywhere, whereas TV promotes solutions which have sparse gradients, i.e. the images are piecewise constant and appear cartoon-like. The latter also leads to the staircase artefact which can be overcome by TGV which promotes piecewise linear solutions. None of these regularisers are able to encode additional information on the location or direction of edges.

1.3 Contributions

The contributions in this chapter are threefold.

Overview over existing methods We provide an overview on existing mathematical models for structural similarity which are related to the shared location or direction of edges. We then discuss various regularisers which promote similarity in this sense.

Higher order models Existing methods focus on incorporating additional information into regularisers modelling first-order smoothness. We extend existing methodology to second-order smoothness using the total generalised variation framework.

Extensive numerical comparison We highlight the properties of the discussed regularisers and the dependence on various parameters using two inverse problems: tomography and super-resolution.

1.4 Related work

1.4.1 Joint reconstruction

One can think of the setting (1) with extra information v as a special case when multiple measurements

$$K_i u_i = f_i \quad i = 1, \dots, m \tag{6}$$

are taken. If $m = 2$ and one inverse problem is considerably less ill-posed, then this can be solved first to guide the inversion of the other. Some of the described models can be extended to the more general case (e.g. an arbitrary number of modalities) or the joint recovery of both/all unknowns, see e.g. [3–9, 12, 38, 41, 56, 58, 63, 75–77, 82, 83, 99], but it is out of the scope of this chapter to provide an overview on those. For an overview up to 2015, see [100]. A few recent contributions are summarized in [101].

Model (6) may include several special cases i) multiple measurements of the same unknown, i.e. $u_i = u$ and ii) measurements correspond to different states of the same unknown, e.g. in dynamic imaging $u_i = u(\cdot, t_i)$. The former case is covered by the standard literature when concatenating the measurements and the systems models, i.e. $(Ku)_i := K_i u$ and $f = (f_1, \dots, f_m)$. The latter has been widely studied in the literature, too, see e.g. [102–104] and references therein. Both of these are in general unrelated to multi-modality imaging.

1.4.2 Other models for similarity

The earliest contributions to structure-promoting regularisers for multi-modality imaging were made in the early 1990s by Leahy and Yan [17] who used a segmentation of an anatomical MRI image to enhance PET reconstruction. This is achieved by carefully handcrafting a regulariser which can encode this information. In this chapter we will use the same strategy but in a continuous setting which is independent of the discretisation and will not rely on a segmentation of the side information v. These ideas were subsequently refined in various directions [18–20, 22–25, 27, 28, 33, 34, 44] of which Bowshers prior [23] remains most popular today.

Other models that can combine information of multiple modalities are based on coupled diffusion [1, 61, 99], level-sets [30], information theoretic priors (joint entropy, mutual information) [21, 26, 29, 37], Bregman distances [49, 65, 66, 105, 106], Bregman iterations [64, 107], the structure tensor [108], joint dictionary learning [47, 78, 109], common edge weighting [41] and deep learning [48]. Most of these methods are very different to what will be described in this chapter. There are some similarities between the methods of this chapter and methods which are based on the Bregman distance of the total variation [49, 64–66, 105–107] but a detailed treatment is outside the scope of this section.

2 Mathematical models for structural similarity

In this section we define mathematical models where we aim to capture the similarities as shown in Figures 1 to 5. We start by explicitly stating two definitions which capture structural similarity which have been used implicitly in the literature. The first is based on the location of edges or the edge set [1–5, 41, 56, 64] and the second is based on direction of edges or the shape of an object [3, 5–9, 12]. The latter is essentially the same as Definition 5.1.6 in [100] except for the degenerate case when either $\nabla u(x) = 0$ or $\nabla v(x) = 0$.

Definition 1 (Structural similarity with edge sets). *Two differentiable images $u, v : \Omega \to \mathbb{R}$ are said to be* structurally similar in the sense of edge sets *if*

$$\mathcal{E}u = \mathcal{E}v \tag{7}$$

where $\mathcal{E}u = \{x \in \Omega \mid \nabla u(x) \neq 0\}$. We also write $u \overset{e}{\sim} v$ to denote that u and v are structurally similar in the sense of edge sets.

Definition 2 (Structural similarity with parallel level sets). *Two differentiable images $u, v : \Omega \to \mathbb{R}$ are said to be* structurally similar in the sense of parallel level sets *if $u \overset{e}{\sim} v$ and for all $x \in \mathcal{E}u$ there is*

$$\nabla u(x) \parallel \nabla v(x). \tag{8}$$

We also write $u \overset{d}{\sim} v$ to denote that u and v are structurally similar in the sense of parallel level sets.

Remark 1. *For smooth images u and v, their gradients are perpendicular to their level sets, i.e. $u^{-1}(s) = \{x \in \Omega \mid u(x) = s\}$. Thus parallel gradients is equivalent to parallel level sets which explains the naming. The notion that the structure of an image is contained in its level sets dates back to [110].*

Remark 2. *By definition, similarity with parallel level sets (Definition 2) is stronger than the definition that only involves edge sets (Definition 1). An example of two images u and v which have the same edge set but do not have parallel level sets is the following. $u, v : \Omega \subset \mathbb{R}^2 \to \mathbb{R}, u(x) = x_1, v(x) = x_2$. Clearly they have the same edge set since $\mathcal{E}u = \mathcal{E}v = \Omega$, but they do not have parallel level sets since $\nabla u(x) = [1, 0]$ but $\nabla v(x) = [0, 1]$.*

Remark 3. *Two images u and v have parallel level sets if and only if $u \overset{e}{\sim} v$ and for all $x \in \mathcal{E}u$ there exists $\alpha \in \mathbb{R}$ such that*

$$\nabla u(x) = \alpha \nabla v(x). \tag{9}$$

Examples of images which have parallel level sets include:

1. Function value transformations. *Let $f : \mathbb{R} \to \mathbb{R}$ be smooth and strictly monotonic, i.e. $f' > 0$ or $f' < 0$. Then $v := f \circ u \overset{d}{\sim} u$. This is readily to be seen from the fact that $\nabla v(x) = f'(u(x))\nabla u(x) \neq 0$ if and only if $\nabla u(x) \neq 0$.*

2. Local function value transformations. *Let* $f_i : \mathbb{R} \to \mathbb{R}$ *be smooth and strictly monotonic and* $u = \sum_i u_i$ *where* u_i *are smooth functions whose gradients have mutually disjoint support. Then* $v := \sum_i f_i \circ u_i \overset{d}{\sim} u.$

Remark 4. *It has been argued in the literature that many multi-modality images* $z : \Omega \to \mathbb{R}^m$ *essentially decompose as*

$$z_i(x) = \tau_i(x)\rho(x) \tag{10}$$

where $\rho(x)$ *describes its structure and* τ *is a material property, see e.g. [63, 111]. Since the material does not change arbitrarily, it is natural to assume that* τ_i *is slowly varying or even piecewise constant. In the latter case, if* x *is such that* $\nabla\tau_i(x) = 0$*, then we have*

$$\nabla z_i(x) = \tau_i(x)\nabla\rho(x)\,, \tag{11}$$

in particular if $\tau_i, \tau_j \neq 0$*, then* $z_i \overset{d}{\sim} z_j$*. This property is also related to the material decomposition in spectral CT, see e.g. [112–114].*

2.1 Measuring structural similarity

Measuring the degree of similarity with respect to the previous two definitions of structural similarity is not easy and we will now discuss a couple of ideas from the literature. Here and for the rest of this chapter, we will make frequent use of the vector-valued representation of a set of images $z : \Omega \to \mathbb{R}^2, z(x) := [u(x), v(x)]$. We denote by J its Jacobian, i.e. $J : \Omega \to \mathbb{R}^{d\times 2}, J_{i,j} = \partial_i z_j$.

With the definition of the Jacobian we see that $u \overset{e}{\sim} v$ if and only if

$$\int_\Omega |J(x)|_0\,\mathrm{d}x = \int_\Omega |\nabla u(x)|_0\,\mathrm{d}x = \int_\Omega |\nabla v(x)|_0\,\mathrm{d}x \tag{12}$$

where $|x|_0 := 1$ if $x \neq 0$ and 0 else.

Similarly, by definition $u \overset{d}{\sim} v$ if and only if $u \overset{e}{\sim} v$ and (a) $\operatorname{rank} J(x) = 1$ for all $x \in \mathcal{E}u$. (a) is equivalent to (b) a vanishing determinant, i.e. $\det J^\top(x)J(x) = 0$. Simple calculations, see e.g. [100], show that

$$\det J^\top(x)J(x) = |\nabla u(x)|^2|\nabla v(x)|^2 - \langle\nabla u(x), \nabla v(x)\rangle^2\,, \tag{13}$$

where we use the notation $\langle x, y\rangle = x^\top y$ for the inner product of two column vectors x and y. In order to get further equivalent statements we turn to the singular values of the Jacobian which are given by

$$\sigma_{1/2}^2(x) = \frac{1}{2}\left[|J(x)|^2 \pm \sqrt{|J(x)|^4 - \det J^\top(x)J(x)}\right] \tag{14}$$

with $|J(x)|^2 = |\nabla u(x)|^2 + |\nabla v(x)|^2$, see e.g. [100]. Since $\sigma_1(x) \geq \sigma_2(x) \geq 0$ we have that (a) holds if and only if (c) the second singular value vanishes, i.e. $\sigma_2(x) = 0$ or (d) the vector of singular vectors $\sigma(x) = [\sigma_1(x), \sigma_2(x)]$ is 1-sparse.

3 Structure-promoting regularisers

Many of the abstract models from the previous section to measure the degree of similarity with respect to the previous two definitions of structural similarity are computationally challenging as they relate to non-convex constraints. In this section we will define convex structure-promoting regularisers which make them computationally tractable.

3.1 Isotropic models

We first look at isotropic models which only depend on gradient magnitudes rather than directions, thus promote structural similarity in the sense of edge sets, Definition 1.
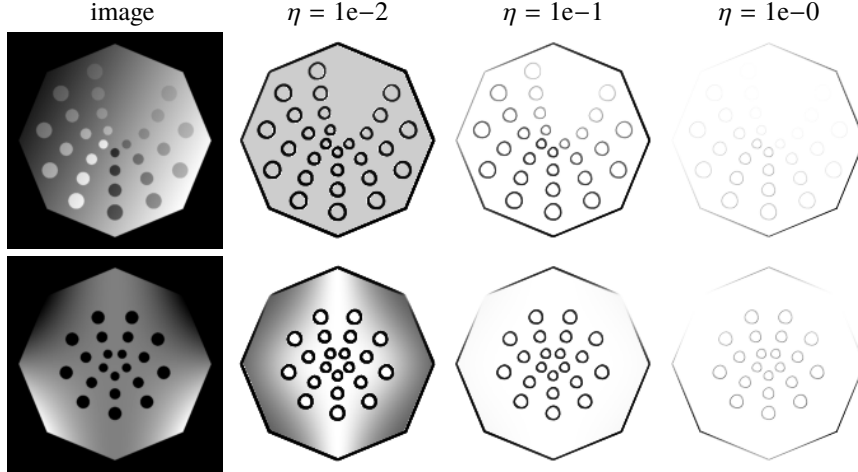
| image | $\eta = 1\mathrm{e}{-}2$ | $\eta = 1\mathrm{e}{-}1$ | $\eta = 1\mathrm{e}{-}0$ |

Figure 6: Influence of the parameter η on estimation of **edge location**. The images on the right show the scalar field $w : \Omega \to [0,1]$ which locally weights the influence of the regulariser, see (18). Here "black" denotes 0 and "white" denotes 1.

First, based on (12) if we approximate $|J(x)|_0$ by $|J(x)|$, then

$$\mathrm{JTV}(u) = \int_\Omega |J(x)| \, \mathrm{d}x = \int_\Omega \sqrt{|\nabla u(x)|^2 + |\nabla v(x)|^2} \, \mathrm{d}x \qquad (15)$$

$$\leq \int_\Omega |\nabla u(x)| + |\nabla v(x)| \, \mathrm{d}x = \mathrm{TV}(u) + \mathrm{TV}(v) \qquad (16)$$

with equality if and only if $\mathcal{E}u \cap \mathcal{E}v = \emptyset$. This regulariser is called *joint total variation* in some communities, see e.g. [3, 5, 11, 56] and *vectorial total variation* in others, see e.g. [2].

Remark 5. *Note that* JTV *has the favourable property that if $\nabla v = 0$, then $\mathrm{JTV}(u) = \mathrm{TV}(u)$, so that it reduces to a well defined regularisation in u in this degenerate case. Note that this property also holds locally.*

Remark 6. *We would also like to note that there is a connection between* JTV *and the singular values of J. Let $\sigma_1, \sigma_2 : \Omega \to [0, \infty)$ be the two singular values of J, then we have*

$$\mathrm{JTV}(u) = \int_\Omega \sqrt{\sigma_1^2(x) + \sigma_2^2(x)} \, \mathrm{d}x \, . \qquad (17)$$

Another strategy to favour edges at similar locations while reducing to a well-defined regulariser in the degenerate case is to introduce local weighting. Let $w : \Omega \to [0,1]$ be an edge indicator function for v such that $w(x) = 1$ when $\nabla v(x) = 0$ and a small value whenever $|\nabla v(x)|$ is large. For example, choose

$$w(x) = \frac{\eta}{\sqrt{\eta^2 + |\nabla v(x)|^2}} \qquad (18)$$

which is illustrated in Figure 6. The figure shows that with a medium η the weight w in (18) shows the main structures of the images so that these can be promoted in the other image. If η is too small, then also unwanted structures are captured in w such as a smooth background variation. If η is too large, then the structures start to disappear.

For regularisers which are based on the image gradient ∇u, the weighting w can be used to favour edges at certain locations by replacing ∇ by $w\nabla$. For instance, for H^1 (3), TV (4) and TGV (5) this strategy results in

$$\mathrm{wH}^1(u) = \int_\Omega |w(x)\nabla u(x)|^2 \, \mathrm{d}x = \int_\Omega w^2(x)|\nabla u(x)|^2 \, \mathrm{d}x \qquad (19)$$

$$\mathrm{wTV}(u) = \int_\Omega |w(x)\nabla u(x)| \, \mathrm{d}x = \int_\Omega w(x)|\nabla u(x)| \, \mathrm{d}x \qquad (20)$$

$$\mathrm{wTGV}(u) = \inf_\zeta \int_\Omega |w(x)\nabla u(x) - \zeta(x)| + \beta |E\zeta(x)| \, \mathrm{d}x \qquad (21)$$
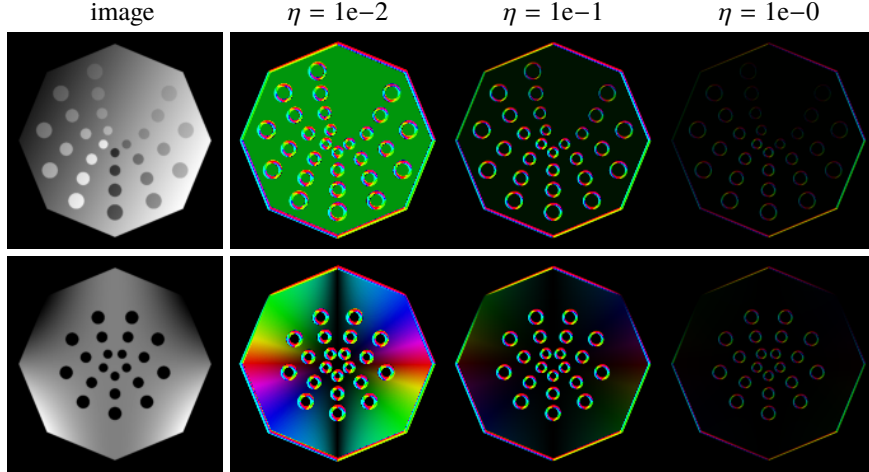
Figure 7: Influence of the parameter η on estimation of **edge location and direction**. The images on the right show the vector field $\xi : \Omega \to \mathbb{R}^d$ which locally defines the influence of the regulariser, see e.g. (22). Here "black" denotes that the magnitude of ξ, i.e. $|\xi(x)|$, is 0 and a bright colour denotes that $|\xi(x)|$ is 1. The colours show the direction of the vector field ξ modulo its sign.

which we will refer to as *weighted squared H^1-semi norm, weighted total variation* and *weighted total generalised variation.* wTV was used in [1, 10, 115]. A variant of wTV has been considered for single modality imaging in [116, 117] and extended to a variant of wTGV [118].

Remark 7. *The parameter η in w, see (18), should be chosen in relation to $|\nabla v(x)|$. A common strategy is to normalise the side information first such that $\sup_{x\in\Omega} |\nabla v(x)| = 1$. Then desirable values of η are usually within the range $[0.01, 1]$.*

3.2   Anisotropic models

The same idea which resulted in isotropically "weighted" variants of common regularisers can be used anisotropically, i.e. by making the local weights vary with direction. Let us denote the anisotropic weighting by $D : \Omega \to \mathbb{R}^{d\times d}$. Similar to the isotropic variant, one would like the weight to become the identity matrix, i.e. $D(x) = I$, when $\nabla v(x) = 0$. In order to promote parallel level sets it is desirable that $D(x)\nabla u(x)$ should be small if $\nabla u(x) \parallel \nabla v(x)$ and $D(x)\nabla u(x) = \nabla u(x)$ if $\nabla u(x) \perp \nabla v(x)$. For example

$$D(x) = I - \gamma \xi(x)\xi^\top(x), \quad \xi(x) = \frac{\nabla v(x)}{\sqrt{\eta^2 + |\nabla v(x)|^2}} \tag{22}$$

for $\gamma \in (0, 1]$ (usually close to 1) and $\eta > 0$ satisfies all of these properties. Clearly if $\nabla v(x) = 0$ then $\xi = 0$ such that $D(x) = I$. Moreover, if $\nabla u(x) \parallel \nabla v(x)$, then there exists an α such that $\nabla u(x) = \alpha \nabla v(x)$ and

$$D(x)\nabla u(x) = \left[I - \frac{\gamma}{\eta^2 + |\nabla v(x)|^2} \nabla v(x) \nabla v^\top(x) \right] \nabla u(x) \tag{23}$$

$$= \left[1 - \frac{\gamma |\nabla v(x)|^2}{\eta^2 + |\nabla v(x)|^2} \right] \nabla u(x). \tag{24}$$

The scalar weighting factor converges to $1 - \gamma$ for $|\nabla v(x)| \to \infty$. Finally, if $\nabla u(x) \parallel \nabla v(x)$, then clearly $D(x)\nabla u(x) = \nabla u(x)$.

The example of the matrix-field $D : \Omega \to \mathbb{R}^{d\times d}$ in (22) is determined by the vector-field $\xi : \Omega \to \mathbb{R}^d$ which we visualise in Figure 7. The colours show the direction of the vector-field modulo its sign (since $\xi(x)\xi^\top(x)$ is invariant to a change of sign) and the brightness indicate its magnitude $|\xi(x)|$. Note that images appear as colour versions of Figure 6 which shows the isotropic weighting w.

Table 1: Examples of first-order structure-promoting regularisers, see (32).

regulariser	definition	$B(x)y$	m	$\phi(x)$
H^1	(3)	y	d	$|x|^2$
wH^1	(19)	$w(x)y$	d	$|x|^2$
dH^1	(25)	$D(x)y$	d	$|x|^2$
TV	(4)	y	d	$|x|$
wTV	(20)	$w(x)y$	d	$|x|$
dTV	(26)	$D(x)y$	d	$|x|$
JTV	(16)	$[y, \xi(x)]$	$d \times 2$	$|x|$
TNV	(31)	$[y, \xi(x)]$	$d \times 2$	$|x|_*$

Using a matrix-field in common regularisers lead to their "directional" variant

$$\mathrm{dH}^1(u) = \int_\Omega |D(x)\nabla u(x)|^2 \, \mathrm{d}x \tag{25}$$

$$\mathrm{dTV}(u) = \int_\Omega |D(x)\nabla u(x)| \, \mathrm{d}x \tag{26}$$

$$\mathrm{dTGV}(u) = \inf_\zeta \int_\Omega |D(x)\nabla u(x) - \zeta(x)| + \beta|E\zeta(x)| \, \mathrm{d}x \,. \tag{27}$$

Remark 8. *There is a connection between the particular choice of the matrix-field D in (22) and the Jacobian J.*

$$|D(x)\nabla u(x)|^2 = |\nabla u(x) - \frac{\gamma}{\eta^2 + |\nabla v(x)|^2} \langle \nabla u(x), \nabla v(x) \rangle \nabla v(x)|^2 \tag{28}$$

$$= |\nabla u(x)|^2 - \frac{2\gamma\eta^2 + \gamma(2 - \gamma)|\nabla v(x)|^2}{(\eta^2 + |\nabla v(x)|^2)^2} \langle \nabla u(x), \nabla v(x) \rangle^2 \,. \tag{29}$$

For $\eta = 0$, $\gamma = 1$ and $|\nabla v(x)| = 1$, then with (13) we have

$$|D(x)\nabla u(x)|^2 = |\nabla u(x)|^2|\nabla v(x)|^2 - \langle \nabla u(x), \nabla v(x) \rangle^2 = \det J^\top(x)J(x) \,. \tag{30}$$

Thus, dH^1 corresponds to penalising the determinant. This regulariser is widely used for joint reconstruction in geophysics under the name cross-gradient *function since it is also the cross product of $\nabla u(x)$ and $\nabla v(x)$, see e.g. [6, 7, 76, 77]. Similarly the dTV used for instance in medical imaging [10, 11, 13, 14, 16, 50] and remote sensing [15] can be seen as penalising the square root of the determinant.*

Another strategy to promote parallel level sets is via nuclear norm of the Jacobian which is defined as $|J(x)|_* = \sum_{i=1}^{\min(d,2)} \sigma_i(x)$ where $\sigma_i(x)$ denotes the ith singular value of $J(x)$. Using the nuclear norm promotes sparse vectors of singular values $\sigma(x) = [\sigma_1(x), \sigma_2(x)]$ and thereby parallel level sets. As a regulariser

$$\mathrm{TNV}(u) = \int_\Omega |J(x)|_* \, \mathrm{d}x \tag{31}$$

this strategy became known as *total nuclear variation*, see [9, 12, 63, 73].

All first-order regularisers of this section can be readily summarised in the following standard form

$$\mathcal{J}(u) = \int_\Omega \phi[B(x)\nabla u(x)] \, \mathrm{d}x \tag{32}$$

where $B(x) : \mathbb{R}^d \to \mathbb{R}^m$ is a an affine transformation and $\phi : \mathbb{R}^m \to \mathbb{R}$. For details how B and ϕ can be chosen for specific regularisers to fit this framework, see Table 1. It is useful for Jacobian-based regularisers to use the reweighted Jacobian $[\nabla u(x), \xi(x)]$ with $\xi(x) = \eta\nabla v(x)$ instead.

4 Algorithmic solution

Note that the solution to variational regularisation (2) with either first- (32) or second-order structural regularisation (5), (21), (27) can be cast into the general non-smooth composite optimisation form

$$\min_x \mathcal{F}(Ax) + \mathcal{G}(x) \tag{33}$$

Table 2: Mapping the variational regularisation models into the composite optimisation framework (33). In all cases we choose $A_1 x = Ku$, $\mathcal{F}_1(y_1) = \mathcal{D}(y_1, b)$ and $\mathcal{G}(x) = \iota_{\geq 0}(u)$.

regulariser	definition	x	$A_2 x$	$A_3 x$	$\mathcal{F}_2(y_2)$	$\mathcal{F}_3(y_3)$
H^1	(3)	u	∇u	-	$\alpha\|y_2\|_2^2$	-
wH^1	(19)	u	$w\nabla u$	-	$\alpha\|y_2\|_2^2$	-
dH^1	(19)	u	$D\nabla u$	-	$\alpha\|y_2\|_2^2$	-
TV	(4)	u	∇u	-	$\alpha\|y_2\|_{2,1}$	-
wTV	(20)	u	$w\nabla u$	-	$\alpha\|y_2\|_{2,1}$	-
dTV	(26)	u	$D\nabla u$	-	$\alpha\|y_2\|_{2,1}$	-
JTV	(16)	u	$[\nabla u, 0]$	-	$\alpha\|y_2 - [0,\xi]\|_{2,1}$	-
TNV	(31)	u	$[\nabla u, 0]$	-	$\alpha\|y_2 - [0,\xi]\|_{*,1}$	-
TGV	(5)	(u,ζ)	$\nabla u - \zeta$	$E\zeta$	$\alpha\|y_2\|_{2,1}$	$\alpha\beta\|y_3\|_{2,1}$
wTGV	(21)	(u,ζ)	$w\nabla u - \zeta$	$E\zeta$	$\alpha\|y_2\|_{2,1}$	$\alpha\beta\|y_3\|_{2,1}$
dTGV	(27)	(u,ζ)	$D\nabla u - \zeta$	$E\zeta$	$\alpha\|y_2\|_{2,1}$	$\alpha\beta\|y_3\|_{2,1}$

with $\mathcal{F}(y) = \sum_{i=1}^n \mathcal{F}_i(y_i)$ and $Ax = [A_1 x, \ldots, A_n x]$, see Table 2. We denote by $\|\cdot\|_{2,1}, \|\cdot\|_2^2$ and $\|\cdot\|_{*,1}$ discretisations of

$$z \mapsto \int_\Omega |z(x)|\, \mathrm{d}x \,, \quad z \mapsto \int_\Omega |z(x)|^2\, \mathrm{d}x \quad \text{and} \quad z \mapsto \int_\Omega |z(x)|_*\, \mathrm{d}x \,. \tag{34}$$

4.1 Algorithm

A popular algorithm to solve (33) and therefore (2) is the primal-dual hybrid gradient (PDHG) [119, 120], see Algorithm 1. It consists of two simple steps only involving basic linear algebra and the evaluation of the operator A and its adjoint A^*. Moreover, it involves the computation of the proximal operator of $\tau\mathcal{G}$ and the convex conjugate of $\sigma\mathcal{F}^*$ where τ and σ are scalar step sizes. The proximal operator of a functional $\mathcal{H}$ is defined as

$$\mathrm{prox}_{\mathcal{H}}(z) := \arg\min_x \left\{ \frac{1}{2}\|x - z\|_2^2 + \mathcal{H}(x) \right\} \,. \tag{35}$$

The proximal operator can be computed in closed-form for $\|\cdot\|_{2,1}$ and $\|\cdot\|_2^2$. It also also be computed in closed-form for $\|\cdot\|_{*,1}$ if either the number channels or the dimension of the domain are strictly less than 5, i.e. $m, d < 5$, see [63] for more details. Note also that the proximal operator of $\alpha\mathcal{F}(\cdot - \xi)$ can be readily computed based on the proximal operator of $\mathcal{F}$. More details on proximal operators, convex conjugates and examples can be found for example in [121–124].

For some applications (e.g. x-ray tomography) a preconditioned [42, 125] or randomised [42, 126] variant can be useful but we will not consider these here for simplicity.

Algorithm 1 Primal-dual hybrid gradient (PDHG) to solve (33). Default values given in brackets.

Input: iterates $x(= 0)$, $y(= 0)$, step size parameter $\rho(= 1)$
Initialize: extrapolation $\overline{x} = x$, step sizes $\sigma = \rho/\|A\|$, $\tau = 0.999/(\rho\|A\|)$

1: **for** $k = 1, \ldots$ **do**
2: $\quad x^+ = \mathrm{prox}_{\tau\mathcal{G}}\left(x - \tau A^* y\right)$
3: $\quad y^+ = \mathrm{prox}_{\sigma\mathcal{F}^*}\left(y + \sigma A(2x^+ - x)\right)$

4.2 Prewhitening

Since the operator norms $\|A_i\|, i = 1, \ldots n$ can vary significantly, it is often advisably to "prewhiten" the problem by recasting it as

$$\min_x \tilde{\mathcal{F}}(\tilde{A}x) + \mathcal{G}(x) \,. \tag{36}$$

with $\tilde{\mathcal{F}}(y) := \sum_{i=1}^n \mathcal{F}_i(\|A_i\| \cdot y_i)$ and $\tilde{A}_i x := A_i x/\|A_i\|$. Then trivially $\|\tilde{A}_i\| = 1, i = 1, \ldots, n$ so that all operator norms are equal. Note that the proximal operator of $\sigma\tilde{\mathcal{F}}$ is simple to compute if the proximal
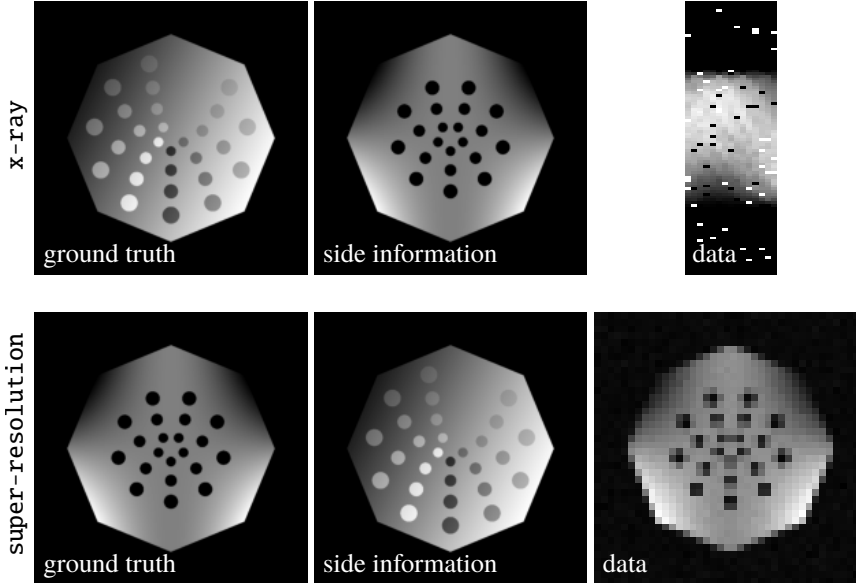
Figure 8: **Test cases for numerical experiments**. Top: x-ray reconstruction from sparse views and failed detectors, bottom: super-resolution by a factor of 5 and Gaussian noise.

operators of $\sigma \mathcal{F}_i, i = 1, \ldots, n$ are simple to compute, since

$$[\text{prox}_{\sigma\tilde{\mathcal{F}}}(y)]_i = \lambda_i^{-1}[\text{prox}_{\sigma\lambda_i^2\mathcal{F}_i}(\lambda_i y_i)], \tag{37}$$

for any $\lambda_i > 0$, see for instance [92, Lemma 6.136].

5 Numerical comparison

This section describes numerical experiments to compare first- and second-order structure-promoting regularisers.

5.1 Software, data and parameters

Software The numerical computations are carried out in Python using ODL (version 1.0.0.dev0) [127] and ASTRA [128, 129] for computing line integrals in the tomography example. The source code which reproduces all experiments in this chapter can be found at `https://github.com/mehrhardt/Multi-Modality-Imaging-with-Structural-Priors`.

Data We consider two test cases with different characteristics, both of which are visualised in Figure 8. The first test case, later referred to as `x-ray`, is parallel beam x-ray reconstruction from only 15 views where additionally some detectors are broken. The latter is modelled by salt-and-pepper noise where 5 % of all detectors are corrupted. We aim to recover an image with domain $[-1, 1]^2$ discretised with 200^2 pixels. The simulated x-ray camera has 100 detectors and a width of 3 in the same dimensions as the image domain. Therefore, the challenges are 1) sparse views, 2) small number of detectors and 3) broken detectors.

The second test case, which we refer to as `super-resolution`, considers the task of super-resolution. Also here we aim to recover an image with domain $[-1, 1]^2$ discretised with 200^2 pixels. The forward operator is integrating over 5^2 pixels, thus mapping images of size 200^2 to images of size 40^2. In addition, Gaussian noise of mean zero and standard deviation of 0.01 is added.

Algorithmic parameters We chose the default value $\rho = 1$ for balancing the step sizes in PDHG and ran the algorithm for 3,000 iterations without choosing a specific stopping criterion.
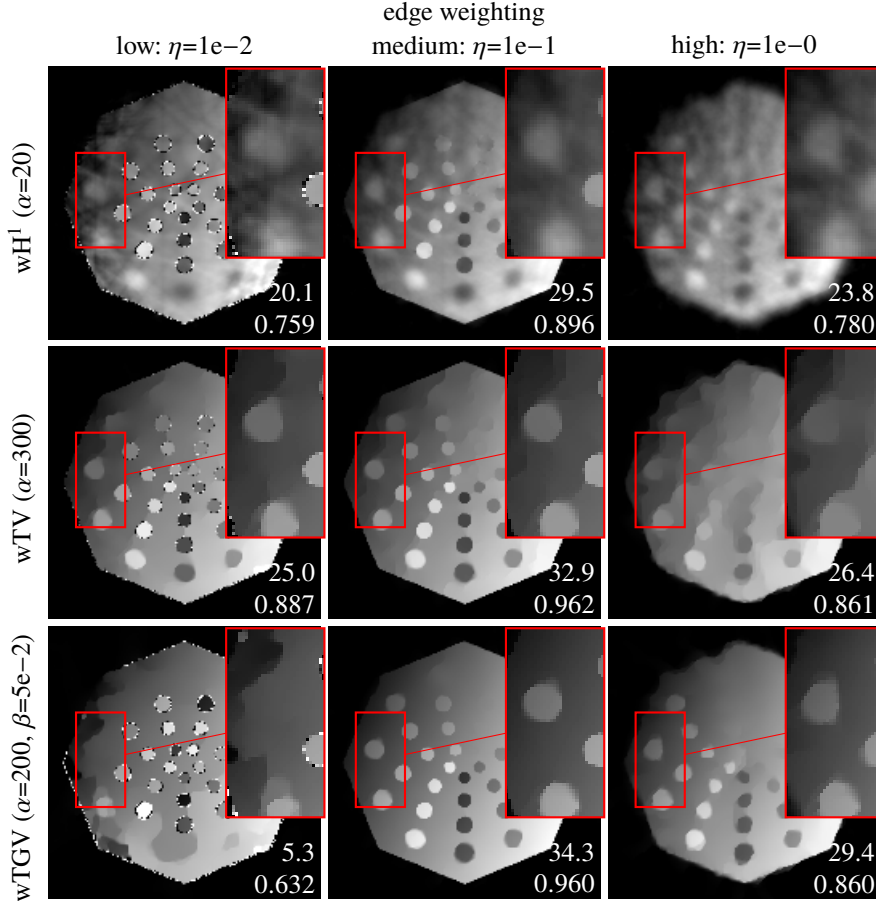
Figure 9: Effect of edge weighting on locally weighted models for test case `x-ray`: increasing edge parameter η from left to right. All other parameters where tuned to maximize the PSNR and visual image quality.

5.2 Numerical results

The multiplicative scaling of an unconstrained optimisation problem is arbitrary, nevertheless we report the absolute values here for completeness. For simplicity, all regularisation parameters are shown as multiples of 1e−4. The figures at the bottom right of each image are PSNR and SSIM.

5.2.1 Test case `x-ray`

Effect of edge weighting All structure-promoting regularisers described in Section 3 have in common that they rely to some extend on the size of edges in the side information, i.e. $|\nabla v(x)|$. For JTV and TNV the actual values of $|\nabla v(x)|$ matter so that a parameter η is needed to correct for this. For all other regularisers a parameter η is needed to decide which edges to trust and which not. The effect of this edge weighting parameter η on all described regularisers is illustrated in Figures 9, 10 and 11. The locally weighted regularisers (i.e. wH^1, wTV and wTGV) and the directional regularisers (i.e. dH^1, dTV and dTGV) have in common that if η is too small, then small artefacts around the edges appear. This effect is more pronounced in locally weighted regularisers. If η is too large, then the structure-promoting effect becomes too small. For joint total variation and total nuclear variation similar effects exist with reverse relationship to η.

Effect of regularisation The effect of the regularisation parameter α on the solution is illustrated in Figures 12, 13 and 14. All regularisers show the same behaviour if α is too small or too large. If the regularisation parameter is chosen too small then artefacts from inverting an ill-posed operator are introduced and if it is chosen too large then all regularisers oversmooth the solution. Note that all structure-promoting regularisers have an increased robustness in areas of shared structures.
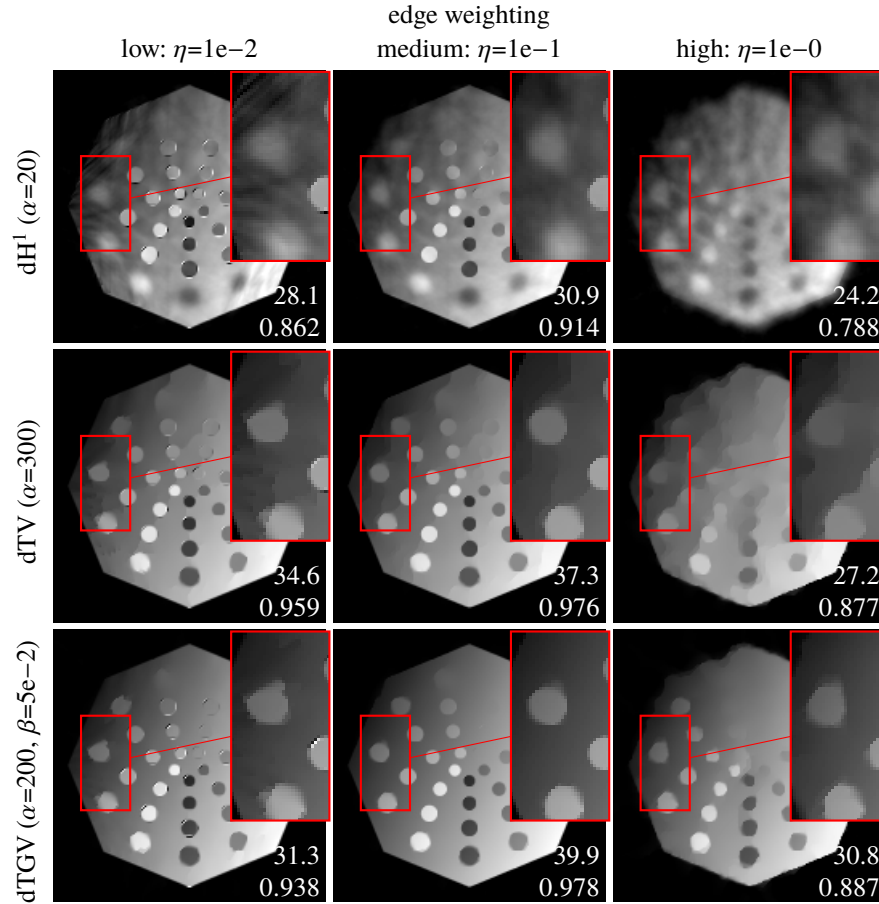
Figure 10: Effect of edge weighting on directional models for test case `x-ray`: increasing edge parameter η from left to right. All other parameters where tuned to maximize the PSNR and visual image quality ($\gamma = 1$).

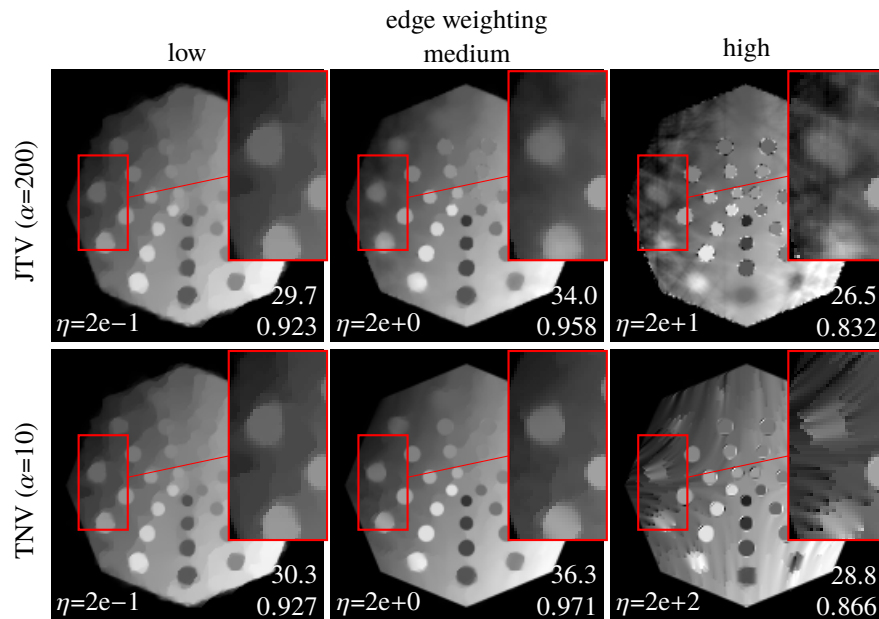

Figure 11: Effect of edge weighting on joint total variation and total nuclear variation for test case `x-ray`: increasing edge parameter η from left to right. All other parameters where tuned to maximise the PSNR and visual image quality.
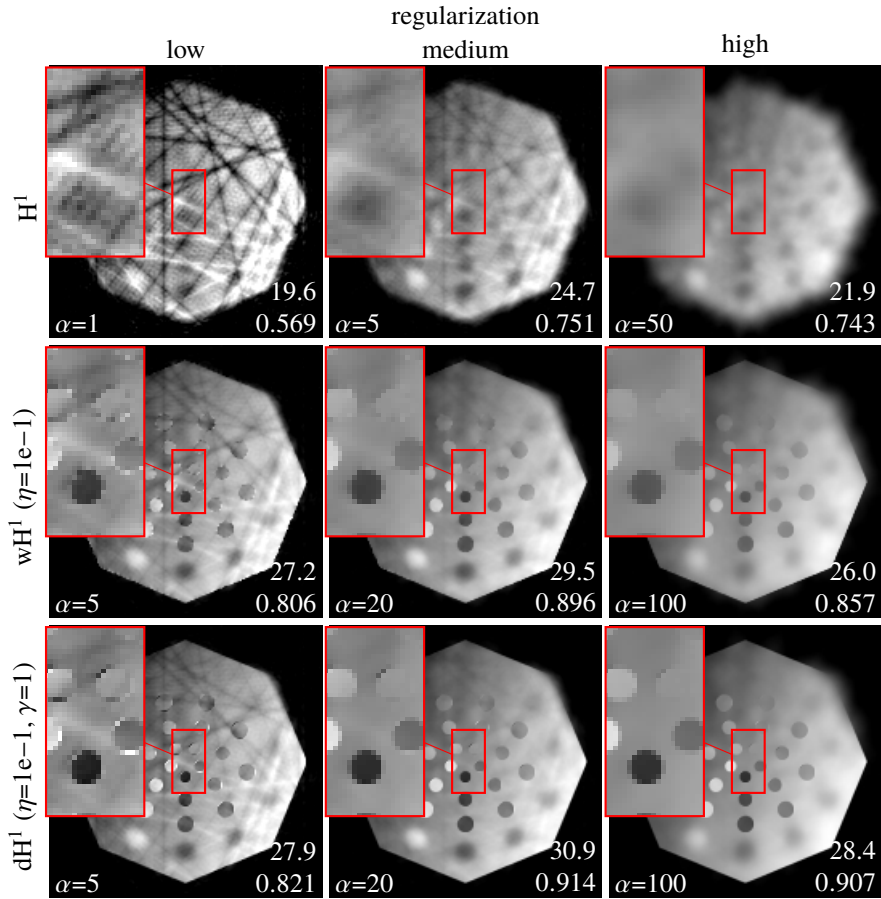
Figure 12: H^1-**semi norm** based structure-promoting regularisers for test case `x-ray`: increasing the regularisation parameter α from left to right. All other parameters where tuned to maximise the PSNR and visual image quality. All regularisers in this figure reduce to the H^1-semi norm in areas where the side information is flat.
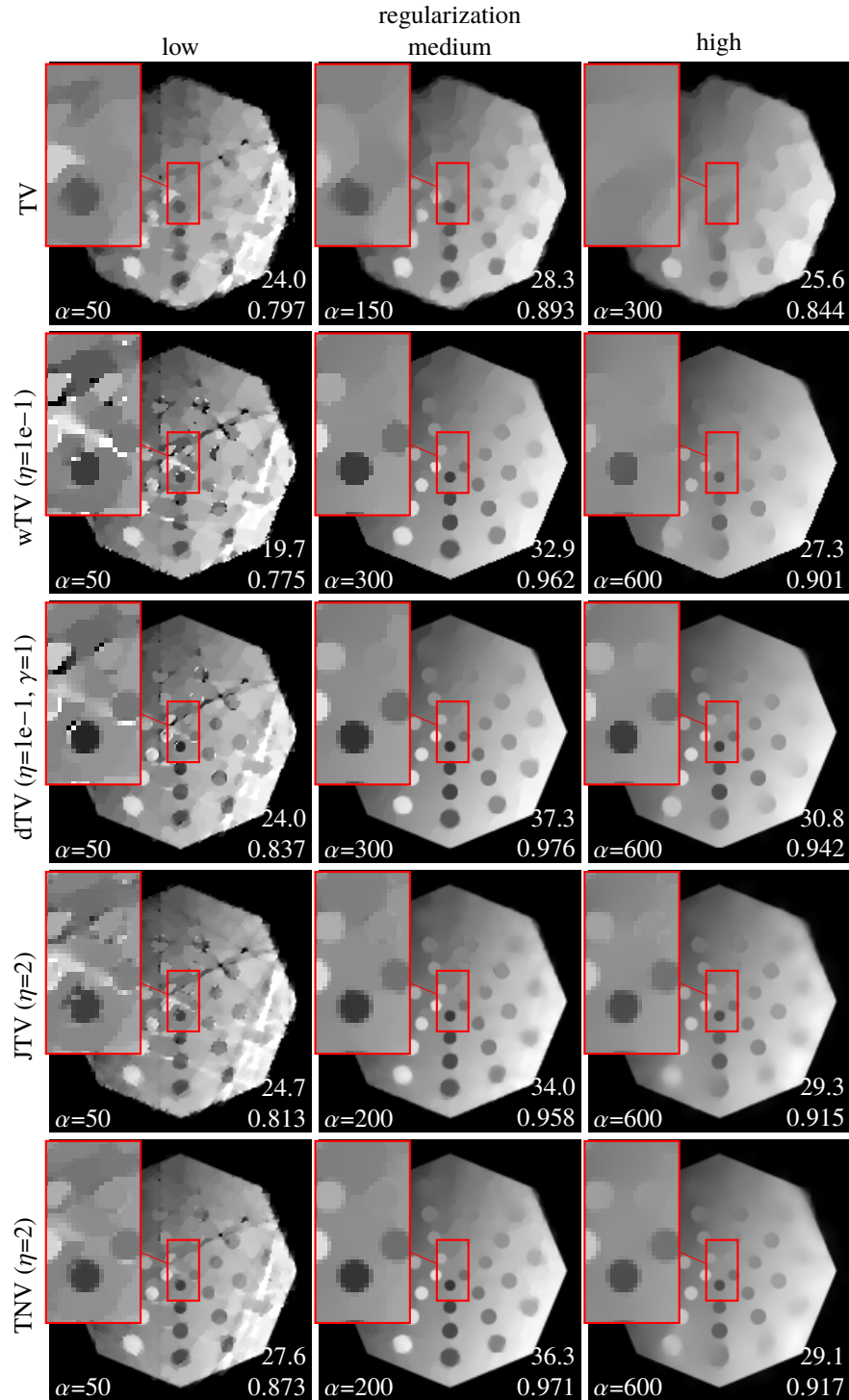
Figure 13: **Total variation** based structure-promoting regularisers for test case `x-ray`: increasing the regularisation parameter α from left to right. All other parameters where tuned to maximise the PSNR and visual image quality. All regularisers in this figure reduce to the total variation in areas where the side information is flat.

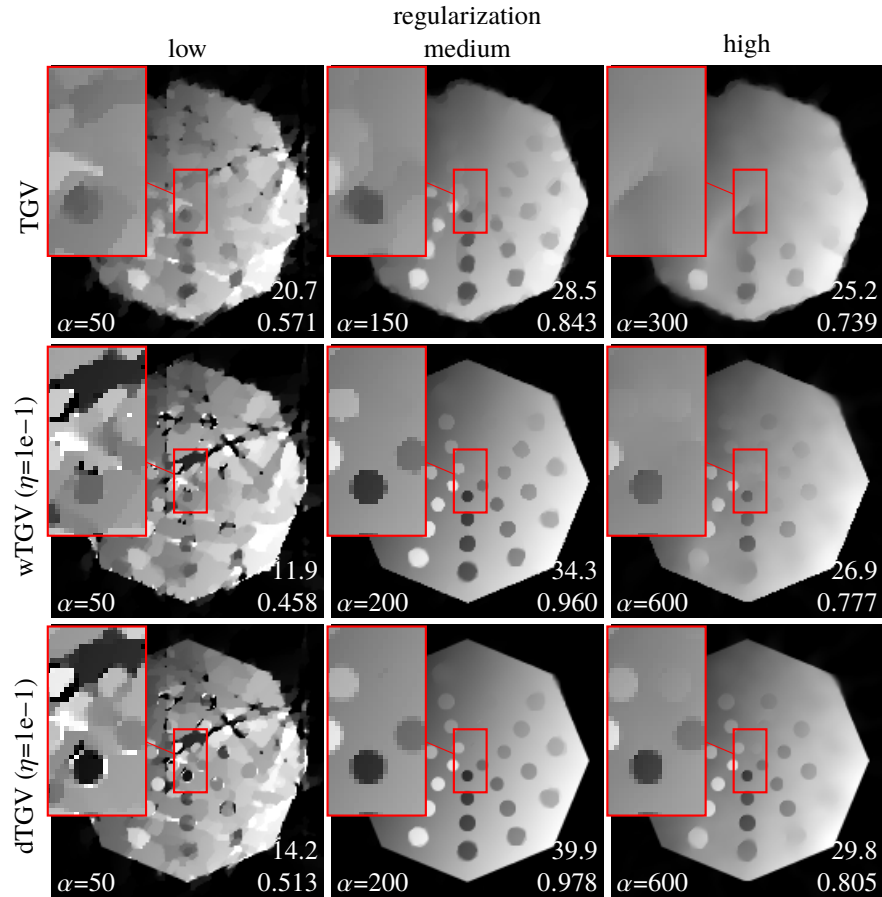Figure 14: **Total generalised variation** based structure-promoting regularisers for test case `x-ray`: increasing the regularisation parameter α from left to right. All other parameters where tuned to maximise the PSNR and visual image quality ($\beta = 5\mathrm{e}{-2}$). All regularisers in this figure reduce to the total generalised variation in areas where the side information is flat.
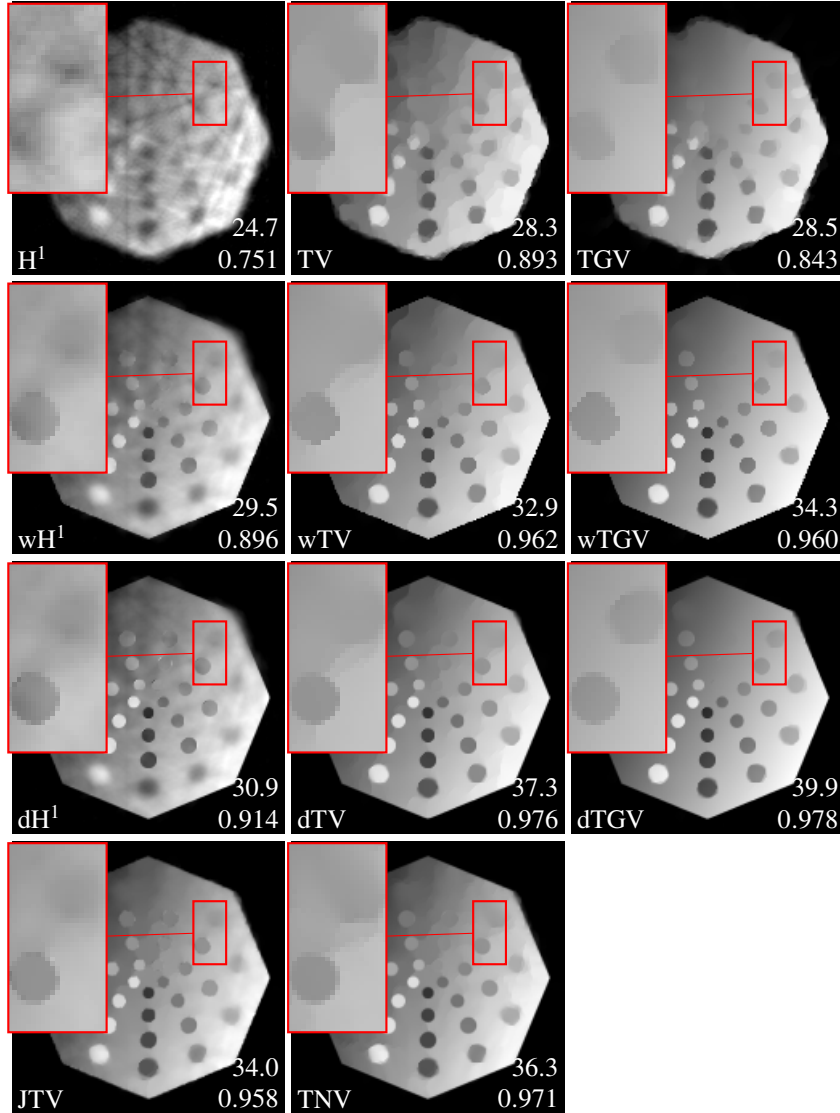
Figure 15: Comparison of structure-promoting regularisers for test case `x-ray`. All parameters where tuned to maximise the PSNR and visual image quality.

Comparison of regularisers All eleven regularisers are compared in Figure 15. It can be seen that the structure-promoting regularisers perform much better in terms of PSNR and SSIM as their non-structure-promoting counterparts. Moreover, one can observe an interesting effect that the structure-promoting regularisers also perform visually better in regions where the structure is not shared, e.g. the outer ring of circles. This effect is most dominant for dTGV where the circle at the top left is clearly visible, while it is difficult to spot for many of the other regularisers.

5.2.2 Test case `super-resolution`

Effect of edge weighting Figures 16, 17 and 18 show the effect of the edge weighting parameter η. One can make similar observations as in Figures 9, 10 and 11 for the test case `x-ray`. In addition, one can observe from the close-ups that if η is too small (or too large for JTV and TNV), then ghosting artefacts may appear. Note that these are present for TNV even for a moderate choice of η.

Comparison of regularisers All regularisers are compared in Figure 19 for the test case `super-resolution`. It can be noted from all images that introducing structural information allows to resolve some of the inner circles which have been merged for regularisers which are not structure-promoting. Moreover, all total generalised variation based regularisers do not perform much better than the total variation based
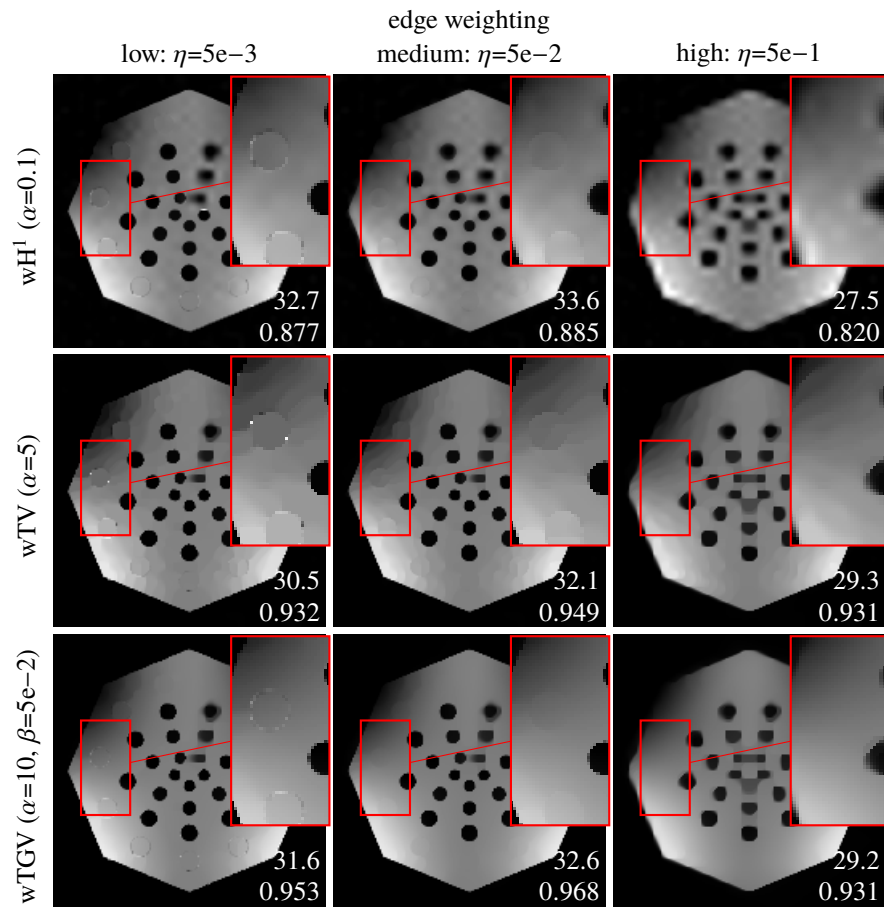
Figure 16: Effect of edge weighting on locally weighted models for test case `super-resolution`: increasing edge parameter η from left to right. All other parameters where tuned to maximise the PSNR and visual image quality.

Figure 17: Effect of edge weighting on directional models for test case `super-resolution`: increasing edge parameter η from left to right. All other parameters where tuned to maximise the PSNR and visual image quality ($\gamma = 0.9$).

Figure 18: Effect of edge weighting on joint total variation and total nuclear variation for test case `super-resolution`: increasing edge parameter η from left to right. All other parameters where tuned to maximise the PSNR and visual image quality.
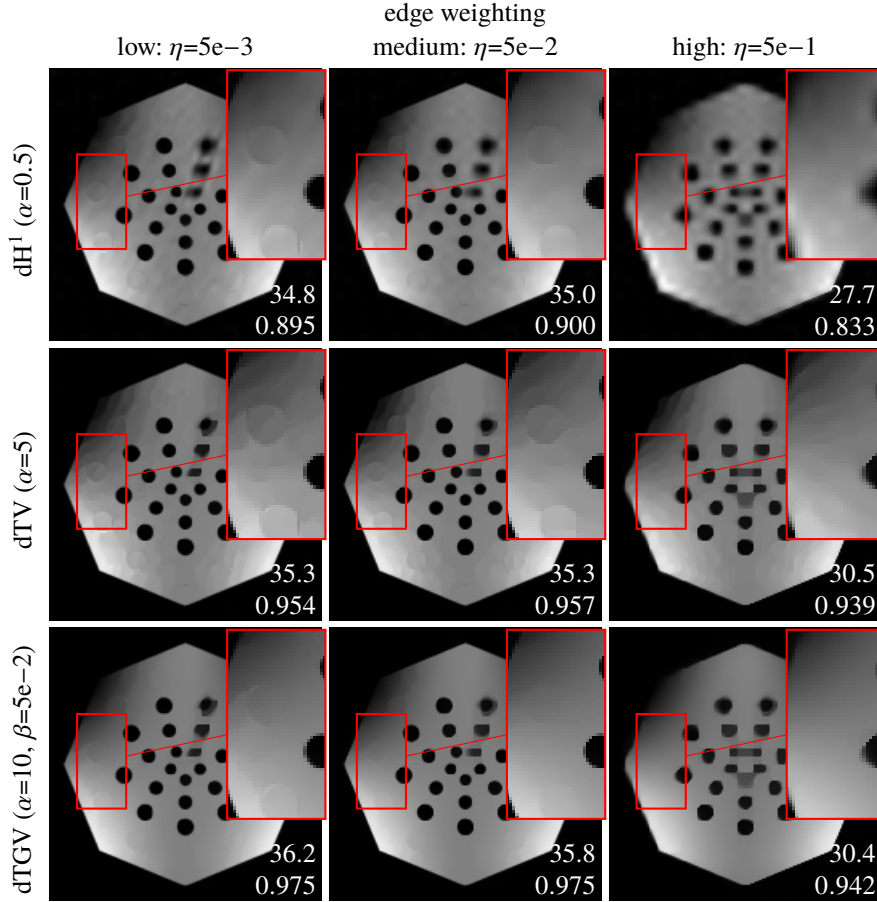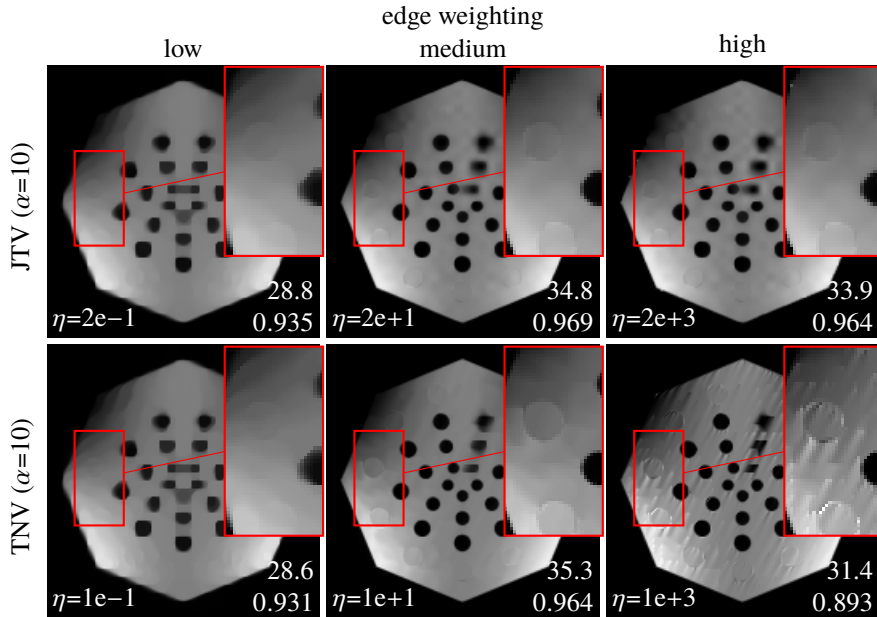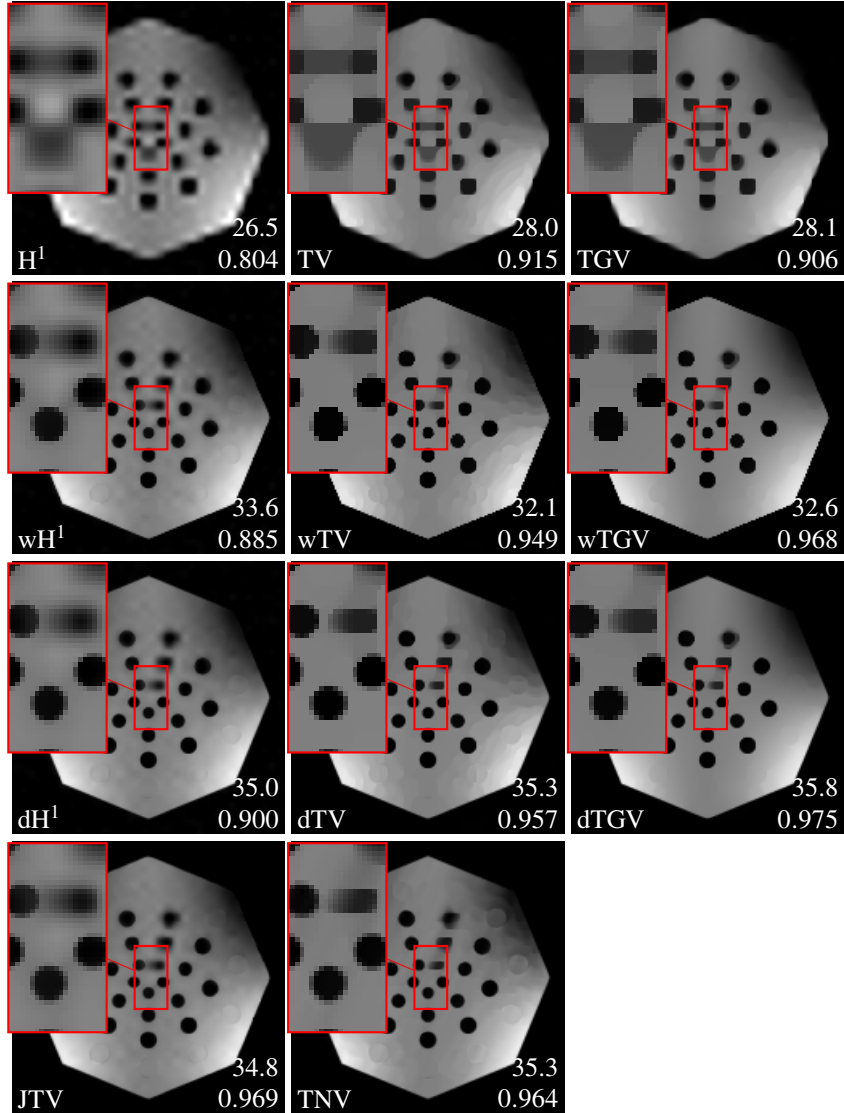
Figure 19: Comparison of structure-promoting regularisers for test case `super-resolution`. All parameters where tuned to maximise the PSNR and visual image quality.

regularisers. The directional regularisers as well as JTV and TNV perform best in terms of PSNR for this example.

5.3 Discussion on computational cost

The median computing times for the numerical experiments are reported in Table 3. The computing time of PDHG is mainly influenced by the dimensions of the models, the proximal operator and the forward model. As can be seen from the table, H^1 and TV are roughly the same fast. TGV which uses a second primal variable in the space of the image gradient is significantly slower with about twice the computational cost. In all three cases, introducing isotropic weights (i.e. wH^1, wTV and wTGV) increases the cost by about 6 seconds, and anisotropic weights (i.e. dH^1, dTV and dTGV) by about 12 seconds. JTV is more costly than dTV but not as costly as TGV. TNV is by far the most costly of all algorithms due to the need to compute singular value decompositions of 2×2-matrices for every pixel.

Since we run PDHG always for 3,000 iterations, we do not report computational time "till convergence" but computational cost for the full 3,000 iterations. It was observed at several occasions, see e.g. [42], that including side information into the regulariser not only improves the reconstruction but also speeds up the algorithmic convergence. Intuitively this can be understood as more information is included into the optimisation problem.

Table 3: Computing times and PSNR for all tested regularisers.

regulariser	computing time		PSNR	
	x-ray	super-resolution	x-ray	super-resolution
H^1	30.43 s	18.34 s	24.7	26.5
wH^1	34.95 s	22.31 s	29.5	33.6
dH^1	40.87 s	27.80 s	30.9	35.0
TV	32.72 s	18.63 s	28.3	28.0
wTV	38.17 s	22.05 s	32.9	32.1
dTV	44.91 s	29.48 s	37.3	35.3
TGV	71.33 s	52.70 s	28.5	28.1
wTGV	77.67 s	58.44 s	34.3	32.6
dTGV	83.34 s	61.65 s	39.9	35.8
JTV	53.04 s	39.05 s	34.0	34.8
TNV	318.45 s	290.42 s	36.3	35.3

Comparing the regularisers regarding their computational time versus image quality trade-off, it can be noted that TNV should not be chosen since it is not better than dTV at 7-10x the computational cost. Whether H^1, TV or TGV based regulariser is desirable depends on each individual application. For each of them, there is a clear trend that one achieves better image quality by introducing more information, i.e. first isotropic information and then anisotropic information, each of which increases their computational cost. However, the increase in computational cost is so small that for most applications the directional variant is likely to be favoured.

6 Conclusions and open problems

This chapter introduced fundamental mathematical concepts on the structure of images and how structural similarity between images can be measured. The fundamental building blocks are the similarity based on edge sets and parallel level sets. These notions lead to several classes of structure-promoting regularisers all of which are convex and thereby lead to tractable optimisation problems when used in variational regularisation for linear inverse problems with convex data fits. While some of the regularisers are smooth and others are non-smooth, the resulting optimisation problem for all of them can be efficiently computed by PDHG. The effectiveness of these regularisers for the promotion of structure has been observed in many applications and was also illustrated in this chapter on two simulation studies.

6.1 Open problems

The mathematical framework for structure-promoting regularisers is by now well established and fairly mature. Open problems reside in practical problems in the translation of these techniques to applications which will also motivate further mathematical research.

Misregistration The biggest open problem is misregistration. All of the described regularisers assume that both images are perfectly aligned. Even in scanners which have two imaging modalities in the same system such as PET-MR, this assumptions is never perfectly fulfilled. This issue has not been addressed much in the literature. In [40], the authors proposed an alternating approach between image reconstruction and image registration with some success. In [15], the problem was formulated as a blind deconvolution problem so that translations can be compensated with a shifted kernel. The resulting optimisation algorithm is related to alternating gradient descent, thus alternates between incremental updates of each variable. This approach seems fairly efficient and robust but is limited to compensating translations and fails to find large deformations. The latter was approached heuristically in [71] but a generally applicable strategy is still to be found.

Extensions beyond two modalities It is natural to consider the case that more than one image is available as side information. For instance, in some remote sensing applications a colour photograph with high spatial resolution is available. Similarly in PET-MR, images of more than one MR sequence

might be available. This setting has also been considered in [39] for a purely discrete model. Some of the regularisers to promote structural similarity in this chapter naturally extend to multiple images as side information, but this has not yet been properly investigated.

Applications   As we illustrated in Section 1, there are many applications where structure-promoting regularisers were already used or are on the horizon. The list of potential target applications grows steadily with more and more multi-modality scanners being introduced. Next to the misregistration mentioned before, the biggest hurdle in real applications is the interpretation of images that were created by fusing information from several modalities. A common question is: "Which edges can I trust?" since often the reconstruction from multi-modality data would be performed on a finer resolution than for the single-modality case. For example, for PET-MR the reconstruction of PET data with an already reconstructed MR image as side information can be performed on the native MRI resolution. The answer might be that such an image should not be interpreted as a PET image, but in fact as a synergistic PET-MR image.

Joint reconstruction   Throughout this chapter the focus was on improving the reconstruction of one image with the aid of another modality used as side information. Since the other image is rarely acquired directly, it is natural to aim to reconstruct both images simultaneously rather than sequentially. While conceptually appealing this strategy leads to many more complications than the approach discussed in this chapter which is sometimes referred to as one-sided reconstruction. While the mathematical framework for one-sided reconstruction is quite mature, the framework for joint reconstruction is despite a lot of research effort in the last 10 years still in its infancy. Fundamental problems like computationally tractable and efficient coupling of modalities is still unsolved. The appealing strategy of making use of the solid mathematical foundations of one-sided reconstruction for joint reconstruction in a mathematical sound and computationally tractable way is still not possible to date.

Acknowledgements

References

[1] S. R. Arridge, V. Kolehmainen, and M. J. Schweiger, "Reconstruction and Regularisation in Optical Tomography," in *Mathematical Methods in Biomedical Imaging and Intensity-Modulated Radiation Therapy (IMRT)* (A. Censor, Y. and Jiang, M. and Louis, ed.), Scuola Normale Superiore, 2008.

[2] X. Bresson and T. F. Chan, "Fast Dual Minimization of the Vectorial Total Variation Norm and Applications to Color Image Processing," *Inverse Problems and Imaging*, vol. 2, pp. 455–484, 11 2008.

[3] E. Haber and M. Holtzman-Gazit, "Model Fusion and Joint Inversion," *Surveys in Geophysics*, pp. 675–695, 8 2013.

[4] F. Knoll, T. Koesters, R. Otazo, F. Boada, and D. K. Sodickson, "Simultaneous MR-PET Reconstruction using Multi Sensor Compressed Sensing and Joint Sparsity," in *International Society for Magnetic Resonance in Medicine*, vol. 22, 2014.

[5] M. J. Ehrhardt, K. Thielemans, L. Pizarro, D. Atkinson, S. Ourselin, B. F. Hutton, and S. R. Arridge, "Joint Reconstruction of PET-MRI by exploiting Structural Similarity," *Inverse Problems*, vol. 31, p. 015001, 1 2015.

[6] L. A. Gallardo and M. A. Meju, "Characterization of Heterogeneous Near-Surface Materials by Joint 2D Inversion of DC Resistivity and Seismic Data," *Geophysical Research Letters*, vol. 30, no. 13, p. 1658, 2003.

[7] L. A. Gallardo and M. A. Meju, "Joint Two-Dimensional DC Resistivity and Seismic Travel Time Inversion with Cross-Gradients Constraints," *Journal of Geophysical Research*, vol. 109, no. B3, pp. 1–11, 2004.

[8] M. J. Ehrhardt and S. R. Arridge, "Vector-Valued Image Processing by Parallel Level Sets," *IEEE Transactions on Image Processing*, vol. 23, no. 1, pp. 9–18, 2014.

[9] D. Rigie and P. La Riviere, "Joint Reconstruction of Multi-Channel, Spectral CT Data via Constrained Total Nuclear Variation Minimization," *Physics in Medicine and Biology*, vol. 60, pp. 1741–1762, 2015.

[10] M. J. Ehrhardt and M. M. Betcke, "Multi-Contrast MRI Reconstruction with Structure-Guided Total Variation," *SIAM Journal on Imaging Sciences*, vol. 9, no. 3, pp. 1084–1106, 2016.

[11] M. J. Ehrhardt, P. J. Markiewicz, M. Liljeroth, A. Barnes, V. Kolehmainen, J. Duncan, L. Pizarro, D. Atkinson, B. F. Hutton, S. Ourselin, K. Thielemans, and S. R. Arridge, "PET Reconstruction with an Anatomical MRI Prior using Parallel Level Sets," *IEEE Transactions on Medical Imaging*, vol. 35, pp. 2189–2199, 8 2016.

[12] F. Knoll, M. Holler, T. Koesters, R. Otazo, K. Bredies, and D. K. Sodickson, "Joint MR-PET Reconstruction using a Multi-Channel Image Regularizer," *IEEE Transactions on Medical Imaging*, vol. 36, no. 1, 2016.

[13] G. Schramm, M. Holler, A. Rezaei, K. Vunckx, F. Knoll, K. Bredies, F. Boada, and J. Nuyts, "Evaluation of Parallel Level Sets and Bowsher's Method as Segmentation-Free Anatomical Priors for Time-of-Flight PET Reconstruction," *IEEE Transactions on Medical Imaging*, vol. 62, no. 2, pp. 590 – 603, 2017.

[14] C. Bathke, T. Kluth, and P. Maass, "Improved Image Reconstruction in Magnetic Particle Imaging using Structural a priori Information," *International Journal of Magnetic Particle Imaging*, vol. 3, no. 1, 2017.

[15] L. Bungert, D. A. Coomes, M. J. Ehrhardt, J. Rasch, R. Reisenhofer, and C.-B. Schönlieb, "Blind Image Fusion for Hyperspectral Imaging with the Directional Total Variation," *Inverse Problems*, vol. 34, no. 4, p. 044003, 2018.

[16] V. Kolehmainen, M. J. Ehrhardt, and S. R. Arridge, "Incorporating Structural Prior Information and Sparsity into EIT using Parallel Level Sets," *Inverse Problems and Imaging*, vol. 13, no. 2, pp. 285–307, 2019.

[17] R. M. Leahy and X. Yan, "Incorporation of Anatomical MR Data for Improved Functional Imaging with PET," in *Information Processing in Medical Imaging*, pp. 105–120, Springer, 1991.

[18] J. E. Bowsher, V. E. Johnson, T. G. Turkington, R. J. Jaszczak, C. E. Floyd, and R. E. Coleman, "Bayesian Reconstruction and Use of Anatomical A Priori Information for Emission Tomography," *IEEE Transactions on Medical Imaging*, vol. 15, no. 5, pp. 673—-686, 1996.

[19] A. Rangarajan, I.-T. Hsiao, and G. Gindi, "A Bayesian Joint Mixture Framework for the Integration of Anatomical Information in Functional Image Reconstruction," *Journal of Mathematical Imaging and Vision*, vol. 12, no. 3, pp. 199–217, 2000.

[20] C. Chan, R. Fulton, D. D. Feng, W. Cai, and S. Meikle, "An Anatomically based Regionally Adaptive Prior for MAP Reconstruction in Emission Tomography," in *IEEE Nuclear Science Symposium and Medical Imaging Conference*, pp. 4137–4141, 2007.

[21] J. Nuyts, "The Use of Mutual Information and Joint Entropy for Anatomical Priors in Emission Tomography," in *IEEE Nuclear Science Symposium and Medical Imaging Conference*, pp. 4149–4154, IEEE, 2007.

[22] C. Comtat, P. E. Kinahan, J. A. Fessler, T. Beyer, D. W. Townsend, M. Defrise, and C. J. Michel, "Clinically Feasible Reconstruction of 3D Whole-Body PET/CT Data using Blurred Anatomical Labels," *Physics in Medicine and Biology*, vol. 47, pp. 1–20, 1 2002.

[23] J. E. Bowsher, H. Yuan, L. W. Hedlund, T. G. Turkington, G. Akabani, A. Badea, W. C. Kurylo, C. T. Wheeler, G. P. Cofer, M. W. Dewhirst, and G. A. Johnson, "Utilizing MRI Information to Estimate F18-FDG Distributions in Rat Flank Tumors," in *IEEE Nuclear Science Symposium and Medical Imaging Conference*, pp. 2488–2492, 2004.

[24] K. Baete, J. Nuyts, W. Van Paesschen, P. Suetens, and P. Dupont, "Anatomical-based FDG-PET Reconstruction for the Detection of Hypo-Metabolic Regions in Epilepsy," *IEEE Transactions on Medical Imaging*, vol. 23, no. 4, pp. 510–9, 2004.

[25] C. Chan, R. Fulton, D. D. Feng, and S. Meikle, "Regularized Image Reconstruction with an Anatomically Adaptive Prior for Positron Emission Tomography," *Physics in Medicine and Biology*, vol. 54, no. 24, pp. 7379–400, 2009.

[26] J. Tang and A. Rahmim, "Bayesian PET Image Reconstruction Incorporating Anato-Functional Joint Entropy," *Physics in Medicine and Biology*, vol. 54, no. 23, pp. 7063–75, 2009.

[27] A. Bousse, S. Pedemonte, D. Kazantsev, S. Ourselin, S. R. Arridge, and B. F. Hutton, "Weighted MRI-based Bowsher Priors for SPECT Brain Image Reconstruction," in *IEEE Nuclear Science Symposium and Medical Imaging Conference*, pp. 3519–3522, 2010.

[28] S. Pedemonte, A. Bousse, B. F. Hutton, S. R. Arridge, and S. Ourselin, "Probabilistic Graphical Model of SPECT/MRI," in *Machine Learning in Medical Imaging*, pp. 167–174, 2011.

[29] S. Somayajula, C. Panagiotou, A. Rangarajan, Q. Li, S. R. Arridge, and R. M. Leahy, "PET Image Reconstruction using Information Theoretic Anatomical Priors," *IEEE Transactions on Medical Imaging*, vol. 30, no. 3, pp. 537–549, 2011.

[30] J. Cheng-Liao and J. Qi, "PET Image Reconstruction with Anatomical Edge Guided Level Set Prior," *Physics in Medicine and Biology*, vol. 56, pp. 6899–6918, 2011.

[31] K. Vunckx, A. Atre, K. Baete, A. Reilhac, C. M. Deroose, K. Van Laere, and J. Nuyts, "Evaluation of Three MRI-based Anatomical Priors for Quantitative PET Brain Imaging," *IEEE Transactions on Medical Imaging*, vol. 31, no. 3, pp. 599–612, 2012.

[32] D. Kazantsev, S. R. Arridge, S. Pedemonte, A. Bousse, K. Erlandsson, B. F. Hutton, and S. Ourselin, "An Anatomically Driven Anisotropic Diffusion Filtering Method for 3D SPECT Reconstruction," *Physics in Medicine and Biology*, vol. 57, no. 12, pp. 3793–3810, 2012.

[33] A. Bousse, S. Pedemonte, B. A. Thomas, K. Erlandsson, S. Ourselin, S. R. Arridge, and B. F. Hutton, "Markov Random Field and Gaussian Mixture for Segmented MRI-based Partial Volume Correction in PET," *Physics in Medicine and Biology*, vol. 57, pp. 6681–705, 10 2012.

[34] B. Bai, Q. Li, and R. M. Leahy, "Magnetic Resonance-guided Positron Emission Tomography Image Reconstruction," *Seminars in Nuclear Medicine*, vol. 43, pp. 30–44, 2013.

[35] G. Delso, S. Furst, B. Jakoby, R. Ladebeck, C. Ganter, S. G. Nekolla, M. Schwaiger, S. I. Ziegler, S. Fürst, B. Jakoby, R. Ladebeck, C. Ganter, S. G. Nekolla, M. Schwaiger, and S. I. Ziegler, "Performance measurements of the Siemens mMR integrated whole-body PET/MR scanner," *Journal of Nuclear Medicine*, vol. 52, pp. 1914–22, dec 2011.

[36] M. J. Ehrhardt, K. Thielemans, L. Pizarro, P. J. Markiewicz, D. Atkinson, S. Ourselin, B. F. Hutton, and S. R. Arridge, "Joint Reconstruction of PET-MRI by Parallel Level Sets," in *IEEE Nuclear Science Symposium and Medical Imaging Conference*, 2014.

[37] J. Tang and A. Rahmim, "Anatomy Assisted PET Image Reconstruction Incorporating Multi-Resolution Joint Entropy," *Physics in Medicine and Biology*, vol. 60, no. 1, pp. 31–48, 2015.

[38] A. Mehranian, M. Belzunce, C. Prieto, A. Hammers, and A. J. Reader, "Synergistic PET and SENSE MR Image Reconstruction using Joint Sparsity Regularization," *IEEE Transactions on Medical Imaging*, vol. 37, no. 1, pp. 20 – 34, 2018.

[39] A. Mehranian, M. A. Belzunce, F. Niccolini, M. Politis, C. Prieto, F. Turkheimer, A. Hammers, and A. J. Reader, "PET Image Reconstruction using Multi-Parametric Anato-Functional," *Phys Med Biol*, 2017.

[40] Y.-j. Tsai, S. Member, A. Bousse, S. Ahn, W. Charles, S. Arridge, B. F. Hutton, S. Member, and K. Thielemans, "Algorithms for Solving Misalignment Issues in Penalized PET / CT Reconstruction Using Anatomical Priors," in *IEEE Nuclear Science Symposium and Medical Imaging Conference Proceedings (NSS/MIC)*, IEEE, 2018.

[41] Y. Zhang and X. Zhang, "PET-MRI joint reconstruction with common edge weighted total variation regularization," *Inverse Problems*, vol. 34, no. 6, p. 065006, 2018.

[42] M. J. Ehrhardt, P. J. Markiewicz, and C.-B. Schönlieb, "Faster PET reconstruction with non-smooth priors by randomization and preconditioning," *Physics in Medicine & Biology*, vol. 64, no. 22, p. 225019, 2019.

[43] D. Deidda, N. A. Karakatsanis, P. M. Robson, Y. J. Tsai, N. Efthimiou, K. Thielemans, Z. A. Fayad, R. G. Aykroyd, and C. Tsoumpas, "Hybrid PET-MR list-mode kernelized expectation maximization reconstruction," *Inverse Problems*, vol. 35, no. 4, 2019.

[44] B. Bilgic, V. K. Goyal, and E. Adalsteinsson, "Multi-Contrast Reconstruction with Bayesian Compressed Sensing," *Magnetic Resonance in Medicine*, vol. 66, pp. 1601–15, 12 2011.

[45] J. Huang, C. Chen, and L. Axel, "Fast Multi-contrast MRI Reconstruction," *Magnetic Resonance Imaging*, vol. 32, no. 10, pp. 1344–52, 2014.

[46] D. K. Sodickson, L. Feng, F. Knoll, M. Cloos, N. Ben-Eliezer, L. Axel, H. Chandarana, K. T. Block, and R. Otazo, "The Rapid Imaging Renaissance: Sparser Samples, Denser Dimensions, and Glimmerings of a Grand Unified Tomography," in *Proceedings of SPIE*, vol. 9417, pp. 94170G1–14, 2015.

[47] P. Song, L. Weizman, J. F. Mota, Y. C. Eldar, and M. R. Rodrigues, "Coupled Dictionary Learning for Multi-Contrast MRI Reconstruction," in *International Conference on Image Processing*, no. 2, pp. 2880–2884, 2018.

[48] L. Xiang, Y. Chen, W. Chang, Y. Zhan, W. Lin, Q. Wang, and D. Shen, "Deep-Learning-Based Multi-Modal Fusion for Fast MR Reconstruction," *IEEE Transactions on Biomedical Engineering*, vol. 66, no. 7, pp. 2105–2114, 2019.

[49] J. Rasch, V. Kolehmainen, R. Nivajarvi, M. Kettunen, O. Gröhn, M. Burger, and E. M. Brinkmann, "Dynamic MRI reconstruction from undersampled data with an anatomical prescan," *Inverse Problems*, vol. 34, no. 7, 2018.

[50] A. J. Obert, M. Gutberlet, A. L. Kern, T. F. Kaireit, R. Grimm, F. Wacker, and J. Vogel-Claussen, "1H-guided reconstruction of 19F gas MRI in COPD patients," *Magnetic Resonance in Medicine*, no. January, pp. 1–11, 2020.

[51] D. Ma, V. Gulani, N. Seiberlich, K. Liu, J. L. Sunshine, J. L. Duerk, and M. A. Griswold, "Magnetic Resonance Fingerprinting," *Nature*, vol. 495, pp. 187–92, mar 2013.

[52] M. Davies, G. Puy, P. Vandergheynst, and Y. Wiaux, "A Compressed Sensing Framework for Magnetic Resonance Fingerprinting," *SIAM Journal on Imaging Sciences*, vol. 7, no. 4, pp. 2623–2656, 2013.

[53] S. Tang, C. Fernandez-Granda, S. Lannuzel, B. Bernstein, R. Lattanzi, M. Cloos, F. Knoll, and J. Asslander, "Multicompartment magnetic resonance fingerprinting," *Inverse Problems*, vol. 34, no. 9, 2018.

[54] G. Dong, M. Hintermüller, and K. Papafitsoros, "Quantitative magnetic resonance imaging: From fingerprinting to integrated physics-based models," *SIAM Journal on Imaging Sciences*, vol. 12, no. 2, pp. 927–971, 2019.

[55] M. Golbabaee, Z. Chen, Y. Wiaux, and M. Davies, "CoverBLIP: accelerated and scalable iterative matched-filtering for magnetic resonance fingerprint reconstruction," *Inverse Problems*, vol. 36, no. 1, p. 015003, 2020.

[56] C. Chen, Y. Li, and J. Huang, "Calibrationless Parallel MRI with Joint Total Variation Regularization," in *Medical Image Computing and Computer-Assisted Intervention*, pp. 106–114, 2013.

[57] E. Ametova, G. Fardell, J. S. Jørgensen, W. R. B. Lionheart, E. Papoutsellis, E. Pasca, D. Sykes, M. Turner, R. Warr, and P. J. Withers, "Core Imaging Library (CIL)," 2019.

[58] G. Sapiro and D. L. Ringach, "Anisotropic Diffusion of Multivalued Images with Applications to Color Filtering," *IEEE Transactions on Image Processing*, vol. 5, pp. 1582–6, 1 1996.

[59] P. Blomgren and T. F. Chan, "Color TV: Total Variation Methods for Restoration of Vector-Valued Images.," *IEEE Transactions on Image Processing*, vol. 7, no. 3, pp. 304–309, 1998.

[60] N. Sochen, R. Kimmel, and R. Malladi, "A General Framework for Low Level Vision," *IEEE Transactions on Image Processing*, vol. 7, no. 3, pp. 310–318, 1998.

[61] D. Tschumperlé and R. Deriche, "Vector-Valued Image Regularization with PDEs: A Common Framework for Different Applications.," *IEEE Transactions on Pattern Analysis and Machine Intelligence*, vol. 27, pp. 506–17, 4 2005.

[62] B. Goldluecke, E. Strekalovskiy, and D. Cremers, "The Natural Vectorial Total Variation Which Arises from Geometric Measure Theory," *SIAM Journal on Imaging Sciences*, vol. 5, pp. 537–563, 1 2012.

[63] K. M. Holt, "Total Nuclear Variation and Jacobian Extensions of Total Variation for Vector Fields," *IEEE Transactions on Image Processing*, vol. 23, no. 9, pp. 3975–3989, 2014.

[64] M. Möller, E.-M. Brinkmann, M. Burger, and T. Seybold, "Color Bregman TV," *SIAM Journal on Imaging Sciences*, vol. 7, pp. 2771–2806, 12 2014.

[65] C. Ballester, V. Caselles, L. Igual, J. Verdera, and B. Rougé, "A Variational Model for P+XS Image Fusion," *International Journal of Computer Vision*, vol. 69, pp. 43–58, 4 2006.

[66] M. Möller, T. Wittman, A. L. Bertozzi, and M. Burger, "A Variational Approach for Sharpening High Dimensional Images," *SIAM Journal on Imaging Sciences*, vol. 5, pp. 150–178, 1 2012.

[67] F. Fang, F. Li, C. Shen, and G. Zhang, "A Variational Approach for Pan-Sharpening," *IEEE Transactions on Image Processing*, vol. 22, no. 7, pp. 2822–2834, 2013.

[68] L. Loncan, L. B. De Almeida, J. M. Bioucas-Dias, X. Briottet, J. Chanussot, N. Dobigeon, S. Fabre, W. Liao, G. A. Licciardi, M. Simoes, J. Y. Tourneret, M. A. Veganzones, G. Vivone, Q. Wei, and N. Yokoya, "Hyperspectral Pansharpening: A Review," *IEEE Geoscience and Remote Sensing Magazine*, vol. 3, no. 3, pp. 27–46, 2015.

[69] N. Yokoya, C. Grohnfeldt, and J. Chanussot, "Hyperspectral and multispectral data fusion: A comparative review of the recent literature," *IEEE Geoscience and Remote Sensing Magazine*, vol. 5, no. 2, pp. 29–56, 2017.

[70] J. Duran, A. Buades, B. Coll, C. Sbert, and G. Blanchet, "A survey of pansharpening methods with a new band-decoupled variational model," *ISPRS Journal of Photogrammetry and Remote Sensing*, vol. 125, pp. 78–105, 2017.

[71] L. Bungert, M. J. Ehrhardt, and R. Reisenhofer, "Robust Blind Image Fusion for Misaligned Hyperspectral Imaging Data," in *Proceedings in Applied Mathematics & Mechanics*, vol. 18, p. e201800033, 2018.

[72] R. Foygel Barber, E. Y. Sidky, T. Gilat Schmidt, and X. Pan, "An algorithm for constrained one-step inversion of spectral CT data," *Physics in Medicine and Biology*, vol. 61, no. 10, pp. 3784–3818, 2016.

[73] D. S. Rigie, A. A. Sanchez, and P. J. La Riviére, "Assessment of vectorial total variation penalties on realistic dual-energy CT data," *Physics in Medicine and Biology*, vol. 62, no. 8, pp. 3284–3298, 2017.

[74] D. Kazantsev, J. S. Jørgensen, M. S. Andersen, W. R. Lionheart, P. D. Lee, and P. J. Withers, "Joint image reconstruction method with correlative multi-channel prior for x-ray spectral computed tomography," *Inverse Problems*, vol. 34, no. 6, 2018.

[75] E. Haber and D. W. Oldenburg, "Joint Inversion: A Structural Approach," *Inverse Problems*, vol. 13, pp. 63–77, 1997.

[76] M. A. Meju, R. L. Mackie, F. Miorelli, A. S. Saleh, and R. V. Miller, "Structurally-tailored 3D anisotropic CSEM resistivity inversion with cross-gradients criterion and simultaneous model calibration," *Geophysics*, vol. 84, no. 6, pp. 1–62, 2019.

[77] L. A. Gallardo and M. A. Meju, "Structure-Coupled Multiphysics Imaging in Geophysical Sciences," *Reviews of Geophysics*, vol. 49, pp. 1–19, 2011.

[78] N. Deligiannis, J. F. Mota, B. Cornelis, M. R. Rodrigues, and I. Daubechies, "Multi-modal dictionary learning for image separation with application in art investigation," *IEEE Transactions on Image Processing*, vol. 26, no. 2, pp. 751–764, 2017.

[79] J. P. Kaipio, V. Kolehmainen, M. Vauhkonen, and E. Somersalo, "Inverse Problems with Structural Prior Information," *Inverse Problems*, vol. 15, no. 3, pp. 713–729, 1999.

[80] Y. Xi, J. Zhao, J. Bennett, M. Stacy, A. Sinusas, and G. Wang, "Simultaneous CT-MRI reconstruction for constrained imaging geometries using structural coupling and compressive sensing," *IEEE Transactions on Biomedical Engineering*, 2015.

[81] P. Elbau, L. Mindrinos, and O. Scherzer, "Quantitative reconstructions in multi-modal photoacoustic and optical coherence tomography imaging," *Inverse Problems*, vol. 34, no. 1, 2018.

[82] Z. W. Di, S. Leyffer, and S. M. Wild, "Optimization-Based Approach for Joint X-Ray Fluorescence and Transmission Tomographic Inversion," *SIAM Journal on Imaging Sciences*, vol. 9, no. 1, pp. 1–23, 2016.

[83] R. Huber, G. Haberfehlner, M. Holler, and K. Bredies, "Total Generalized Variation regularization for multi-modal electron tomography," *Nanoscale*, pp. 1–38, 2019.

[84] G. Wang, J. Zhang, H. Gao, V. Weir, H. Yu, W. Cong, X. Xu, H. Shen, J. Bennett, M. Furth, Y. Wang, and M. Vannier, "Towards Omni-Tomography - Grand Fusion of Multiple Modalities for Simultaneous Interior Tomography," *PloS one*, vol. 7, p. e39700, jan 2012.

[85] W. M. Wells III, P. Viola, H. Atsumi, S. Nakajima, and R. Kikinis, "Multi-Modal Volume Registration by Maximization of Mutual Information," *Medical Image Analysis*, vol. 1, no. 1, pp. 35–51, 1996.

[86] F. Maes, A. Collignon, D. Vandermeulen, G. Marchal, and P. Suetens, "Multimodality Image Registration by Maximization of Mutual Information," *IEEE Transactions on Medical Imaging*, vol. 16, pp. 187–98, apr 1997.

[87] J. P. W. Pluim, J. B. A. Maintz, and M. A. Viergever, "Image Registration by Maximization of Combined Mutual Information and Gradient Information," *IEEE Transactions on Medical Imaging*, vol. 19, no. 8, pp. 809–14, 2000.

[88] E. Haber and J. Modersitzki, "Intensity Gradient based Registration and Fusion of Multi-Modal Images," in *Medical Image Computing and Computer-Assisted Intervention*, vol. 46, pp. 726–733, Berlin Heidelberg: Springer-Verlag, 2006.

[89] H. W. Engl, M. Hanke, and A. Neubauer, *Regularization of Inverse Problems*. Mathematics and Its Applications, Springer, 1996.

[90] O. Scherzer, M. Grasmair, H. Grossauer, M. Haltmeier, and F. Lenzen, *Variational Methods in Imaging*, vol. 167. 2008.

[91] K. Ito and B. Jin, *Inverse Problems - Tikhonov Theory and Algorithms*. World Scientific Publishing, 2014.

[92] K. Bredies and D. A. Lorenz, *Mathematical Image Processing*. Birkhäuser Basel, 1 ed., 2018.

[93] M. Benning and M. Burger, "Modern regularization methods for inverse problems," *Acta Numerica*, vol. 27, pp. 1–111, 2018.

[94] L. I. Rudin, S. Osher, and E. Fatemi, "Nonlinear Total Variation based Noise Removal Algorithms," *Physica D: Nonlinear Phenomena*, vol. 60, no. 1, pp. 259–268, 1992.

[95] M. Burger and S. Osher, "A Guide to the TV Zoo," in *Level Set and PDE Based Reconstruction Methods in Imaging*, vol. 2090 of *Lecture Notes in Mathematics*, pp. 1–70, Springer, 2013.

[96] K. Bredies, K. Kunisch, and T. Pock, "Total Generalized Variation," *SIAM Journal on Imaging Sciences*, vol. 3, no. 3, pp. 492–526, 2010.

[97] K. Bredies and M. Holler, "Regularization of Linear Inverse Problems with Total Generalized Variation," *Journal of Inverse and Ill-Posed Problems*, vol. 22, no. 6, pp. 871–913, 2014.

[98] K. Bredies and M. Holler, "A TGV-Based Framework for Variational Image Decompression, Zooming, and Reconstruction. Part II: Numerics," *SIAM Journal on Imaging Sciences*, vol. 8, no. 4, pp. 2851–2886, 2015.

[99] S. R. Arridge and A. Simmons, "Multi-Spectral Probabilistic Diffusion Using Bayesian Classification," in *Scale-Space Theories in Computer Vision* (B. M. ter Haar Romeny, L. Florack, J. J. Koenderink, and M. A. Viergever, eds.), pp. 224–235, Berlin: Springer, 1997.

[100] M. J. Ehrhardt, *Joint Reconstruction for Multi-Modality Imaging with Common Structure*. Phd thesis, University College London, 2015.

[101] S. R. Arridge, M. Burger, and M. J. Ehrhardt, "Preface to special issue on joint reconstruction and multi-modality / multi-spectral imaging," *Inverse Problems*, vol. 36, p. 020302, 2020.

[102] U. Schmitt and A. K. Louis, "Efficient algorithms for the regularization of dynamic inverse problems: I. Theory," *Inverse Problems*, vol. 18, no. 3, pp. 645–658, 2002.

[103] U. Schmitt, A. K. Louis, C. Wolters, and M. Vaukhonen, "Efficient algorithms for the regularization of dynamic inverse problems: II. Applications," *Inverse Problems*, vol. 18, no. 3, pp. 659–676, 2002.

[104] T. Schuster, B. Hahn, and M. Burger, "Dynamic inverse problems: Modelling - Regularization - numerics," *Inverse Problems*, vol. 34, no. 4, 2018.

[105] V. Estellers, J. Thiran, and X. Bresson, "Enhanced Compressed Sensing Recovery With Level Set Normals," *IEEE Transactions on Image Processing*, vol. 22, pp. 2611–2626, 7 2013.

[106] D. Kazantsev, W. R. B. Lionheart, P. J. Withers, and P. D. Lee, "Multimodal Image Reconstruction using Supplementary Structural Information in Total Variation Regularization," *Sensing and Imaging*, vol. 15, p. 97, 1 2014.

[107] J. Rasch, E.-M. Brinkmann, and M. Burger, "Joint Reconstruction via Coupled Bregman Iterations with Applications to PET-MR Imaging," *Inverse Problems*, vol. 34, no. 1, p. 014001, 2018.

[108] V. Estellers, S. Soatto, and X. Bresson, "Adaptive Regularization With the Structure Tensor," *IEEE Transactions on Image Processing*, vol. 24, no. 6, pp. 1777–1790, 2015.

[109] P. Song, X. Deng, J. F. C. Mota, N. Deligiannis, P.-L. Dragotti, and M. Rodrigues, "Multimodal Image Super-resolution via Joint Sparse Representations induced by Coupled Dictionaries," *IEEE Transactions on Computational Imaging*, pp. 1–1, 2019.

[110] V. Caselles, B. Coll, and J.-M. Morel, "Geometry and Color in Natural Images," *Journal of Mathematical Imaging and Vision*, vol. 16, no. Section 2, pp. 89–105, 2002.

[111] R. Kimmel, R. Malladi, and N. Sochen, "Images as Embedded Maps and Minimal Surfaces: Movies, Color, Texture, and Volumetric Medical Images," *International Journal of Computer Vision*, vol. 39, no. 2, pp. 111–129, 2000.

[112] J. A. Fessler, I. Elbakri, P. Sukovic, and N. H. Clinthorne, "Maximum-likelihood dual-energy tomographic image reconstruction," in *SPIE: Medical Imaging*, vol. 4684, pp. 1–25, 2002.

[113] B. Heismann, B. Schmidt, and T. Flohr, *Spectral Computed Tomography*. SPIE Press, 2012.

[114] Y. Long and J. A. Fessler, "Multi-material decomposition using statistical image reconstruction for spectral CT," *IEEE Transactions on Medical Imaging*, vol. 33, no. 8, pp. 1614–1626, 2014.

[115] F. Lenzen and J. Berger, "Solution-Driven Adaptive Total Variation Regularization," in *SSVM*, pp. 203–215, 2015.

[116] M. Hintermüller and M. M. Rincon-Camacho, "Expected Absolute Value Estimators for a Spatially Adapted Regularization Parameter Choice Rule in L1-TV-based Image Restoration," *Inverse Problems*, vol. 26, no. 8, p. 085005, 2010.

[117] Y. Dong, M. Hintermüller, and M. M. Rincon-Camacho, "Automated Regularization Parameter Selection in Multi-Scale Total Variation Models for Image Restoration," *Journal of Mathematical Imaging and Vision*, vol. 40, no. 1, pp. 82–104, 2011.

[118] K. Bredies, Y. Dong, and M. Hintermüller, "Spatially Dependent Regularization Parameter Selection in Total Generalized Variation Models for Image Restoration," *International Journal of Computer Mathematics*, pp. 1–15, 2012.

[119] E. Esser, X. Zhang, and T. F. Chan, "A General Framework for a Class of First Order Primal-Dual Algorithms for Convex Optimization in Imaging Science," *SIAM Journal on Imaging Sciences*, vol. 3, no. 4, pp. 1015–1046, 2010.

[120] A. Chambolle and T. Pock, "A First-Order Primal-Dual Algorithm for Convex Problems with Applications to Imaging," *Journal of Mathematical Imaging and Vision*, vol. 40, no. 1, pp. 120–145, 2011.

[121] H. H. Bauschke and P. L. Combettes, *Convex Analysis and Monotone Operator Theory in Hilbert Spaces*. 2011.

[122] P. L. Combettes and J. C. Pesquet, "Proximal splitting methods in signal processing," *Springer Optimization and Its Applications*, vol. 49, pp. 185–212, 2011.

[123] N. Parikh and S. P. Boyd, "Proximal Algorithms," *Foundations and Trends in Optimization*, vol. 1, no. 3, pp. 123–231, 2014.

[124] A. Chambolle and T. Pock, "An Introduction to Continuous Optimization for Imaging," *Acta Numerica*, vol. 25, pp. 161–319, 2016.

[125] T. Pock and A. Chambolle, "Diagonal Preconditioning for First Order Primal-Dual Algorithms in Convex Optimization," in *Proceedings of the IEEE International Conference on Computer Vision*, pp. 1762–1769, 2011.

[126] A. Chambolle, M. J. Ehrhardt, P. Richtárik, and C.-B. Schönlieb, "Stochastic Primal-Dual Hybrid Gradient Algorithm with Arbitrary Sampling and Imaging Applications," *SIAM Journal on Optimization*, vol. 28, no. 4, pp. 2783–2808, 2018.

[127] J. Adler, H. Kohr, and O. Öktem, "Operator Discretization Library (ODL)," 1 2017.

[128] W. van Aarle, W. J. Palenstijn, J. De Beenhouwer, T. Altantzis, S. Bals, K. J. Batenburg, and J. Sijbers, "The ASTRA Toolbox: A platform for advanced algorithm development in electron tomography," *Ultramicroscopy*, vol. 157, pp. 35–47, 2015.

[129] W. van Aarle, W. J. Palenstijn, J. Cant, E. Janssens, F. Bleichrodt, A. Dabravolski, J. De Beenhouwer, K. Joost Batenburg, and J. Sijbers, "Fast and flexible X-ray tomography using the ASTRA toolbox," *Optics Express*, vol. 24, no. 22, p. 25129, 2016.